

## Coulomb stress accumulation along the San Andreas Fault system

Bridget Smith and David Sandwell

Institute for Geophysics and Planetary Physics, Scripps Institution of Oceanography, La Jolla, California, USA

Received 2 August 2002; revised 16 January 2003; accepted 18 February 2003; published 11 June 2003.

[1] Stress accumulation rates along the primary segments of the San Andreas Fault system are computed using a three-dimensional (3-D) elastic half-space model with realistic fault geometry. The model is developed in the Fourier domain by solving for the response of an elastic half-space due to a point vector body force and analytically integrating the force from a locking depth to infinite depth. This approach is then applied to the San Andreas Fault system using published slip rates along 18 major fault strands of the fault zone. GPS-derived horizontal velocity measurements spanning the entire  $1700 \times 200$  km region are then used to solve for apparent locking depth along each primary fault segment. This simple model fits remarkably well (2.43 mm/yr RMS misfit), although some discrepancies occur in the Eastern California Shear Zone. The model also predicts vertical uplift and subsidence rates that are in agreement with independent geologic and geodetic estimates. In addition, shear and normal stresses along the major fault strands are used to compute Coulomb stress accumulation rate. As a result, we find earthquake recurrence intervals along the San Andreas Fault system to be inversely proportional to Coulomb stress accumulation rate, in agreement with typical coseismic stress drops of 1–10 MPa. This 3-D deformation model can ultimately be extended to include both time-dependent forcing and viscoelastic response. *INDEX TERMS*: 1206 Geodesy and Gravity: Crustal movements—interplate (8155); 1242 Geodesy and Gravity: Seismic deformations (7205); 3210 Mathematical Geophysics: Modeling; 8164 Tectonophysics: Stresses—crust and lithosphere; 8199 Tectonophysics: General or miscellaneous; *KEYWORDS*: San Andreas Fault, Coulomb stress, crustal deformation, SCEC velocities, crustal stress

**Citation:** Smith, B., and D. Sandwell, Coulomb stress accumulation along the San Andreas Fault system, *J. Geophys. Res.*, 108(B6), 2296, doi:10.1029/2002JB002136, 2003.

### 1. Introduction

[2] The San Andreas Fault (SAF) system, spanning over 1700 km from the Mendocino Triple Junction in the north to the Gulf of California in the south, defines the complex tectonic boundary between the Pacific and North American plates. As the two plates slide past each other, the SAF system accommodates  $\sim 35$ – $50$  mm/yr of relative plate motion that is distributed across a 200 km wide zone [Working Group on California Earthquake Probabilities (WGCEP), 1995, 1999]. The SAF system is composed of an intricate network of subfaults, each of varying geometry, locking depth, and associated failure properties. Earthquake recurrence intervals also vary dramatically along the SAF system subfaults, ranging from 20 years to over 300 years. In order to better understand the earthquake cycle and also help constrain faulting models of the San Andreas Fault system, geodetic measurements of interseismic, postseismic, and coseismic deformation are continually collected along the entire North American-Pacific plate boundary.

[3] While many previous studies of the SAF region have developed local fault slip models to match regional geodetic observations of surface displacement [Savage and Burford, 1973; Savage et al., 1979; King et al., 1987; Li and Lim,

1988; Eberhart-Phillips et al., 1990; Savage, 1990; Lisowski et al., 1991; Feigl et al., 1993; Savage and Lisowski, 1993; Freymueller et al., 1999; Burgmann et al., 2000; Murray and Segall, 2001], our objectives are somewhat different in that we investigate the steady state behavior of the entire San Andreas Fault system. By constraining relative plate motion, maintaining appropriate fault geometry, and implementing geodetic measurements spanning the entire system, we are able to model three-dimensional (3-D) deformation and calculate stress accumulation. First, we investigate whether a single far-field plate velocity can be partitioned among parallel strands in order to accurately model near-field geodetic measurements. Second, we establish spatial variations in apparent locking depth along the main segments of the SAF system. Finally, we use our model to estimate secular buildup in Coulomb stress within the seismogenic layer and accumulation of scalar seismic moment.

[4] The primary purpose for developing our model is to estimate Coulomb stress accumulation rate and to explore its relevancy to earthquake occurrence and failure potential. Following the assumption that major earthquakes typically produce stress drops on the order of 1–10 MPa, estimates of Coulomb stress accumulation rate can provide an upper bound on the recurrence interval of a particular fault segment. Furthermore, recent studies of induced Coulomb stress changes propose that earthquakes may be triggered by stress changes as small as 0.1 MPa [King et al., 1994;

Stein *et al.*, 1994; Fialko and Simons, 2000; King and Cocco, 2001; Zeng, 2001]. High Coulomb stress accumulation rate has also been linked to areas of surface creep [Savage and Lisowski, 1993]. A better understanding of such stress release processes at major plate boundaries, along with estimates of seismic moment magnitude, have also been the focus of recent earthquake hazard potential studies [WGCEP, 1995, 1999; Working Group on Northern California Earthquake Potential (WGNCEP), 1996]. In this analysis, we inspect the role of locking depth, fault geometry, and paralleling fault strands on accumulating interseismic stress along San Andreas Fault system, and investigate how such accumulation is related to shallow fault creep, earthquake recurrence interval, and seismic moment accumulation.

## 2. Fourier Solution to 3-D Body Force Model

[5] For the last several decades, the most commonly used analytic models of fault-induced deformation have been based on the dislocation solutions of Chinnery [1961, 1963], Rybicki [1973], and Okada [1985, 1992]. The latter provide analytic expressions for stress, strain, and displacement in an elastic half-space due to a displacement discontinuity. While these dislocation models are accurate and computationally efficient when applied to individual faults or small fault systems, they may become computationally prohibitive when representing fault geometry over the entire North American-Pacific plate boundary. For example,  $4 \times 10^5$  model calculations are required for 1000 GPS measurements and 400 fault patches. Modeling of InSAR observations could easily require  $4 \times 10^9$  model calculations. However, if model calculations are performed in the spectral domain, the computational effort is substantially reduced. Rather than calculate the Fourier transform of the analytic solutions mentioned above, we instead solve the 3-D elasticity equations in the wave number domain and then inverse Fourier transform to obtain space domain solutions. The key elements of our model derivation are summarized in Appendix A. In the two-dimensional case, our model matches the classical arctangent solution of Weertman [1964], both analytically and numerically (Appendix A). While this elastic half-space model currently ignores crustal heterogeneities and does not explicitly incorporate non-elastic rheology below the brittle-ductile transition, it produces reasonable estimates of first-order tectonic features comparable to other simple models [Savage and Burford, 1973].

[6] To summarize our analytic approach (Appendix A), the elasticity equations are used to derive a set of transfer functions (in the wave number domain) for the 3-D displacement of an elastic half-space due to an arbitrary distribution of vector body forces. The numerical components of this approach involve generating a grid of force couples that simulate complex fault geometry, taking the 2-D Fourier transform of the grid, multiplying by the appropriate transfer function, and finally inverse Fourier transforming. The force model must be designed to match the velocity difference across the plate boundary and have zero net force and zero net moment. There is a similar requirement in gravity modeling, where mass balance is achieved by imposing isostatic compensation and making the grid

dimensions several times larger than the longest length scale in the system (e.g., flexural wavelength or lithospheric thickness). For this fault model, the characteristic length scale is the locking depth of the fault. The key is to construct a model representing a complicated fault system where the forces and moments are balanced. Our numerical approach is as follows:

[7] 1. Develop a force couple segment from the analytic derivative of a Gaussian approximation to a line segment as described in Appendix A; this ensures exact force balance. For an accurate simulation, the half width of the Gaussian must be greater than the grid size but less than the locking depth.

[8] 2. Construct a complicated force couple model using digitized fault segments. For each segment, the strength of the couple is proportional to the long-term slip rate on the fault segment and the direction of the couple is parallel to the overall plate boundary direction (not the local fault direction). This simulates the far-field plate tectonic force couple. Because the model has force couples, the vector sum of all of the forces in the model is zero but there is a large unbalanced moment because all of the force couples act in the same direction.

[9] 3. Double the grid size and place a mirror image of the force couple distribution in the mirror grid so that the moment due to the image fault exactly balances the moment due to the real fault. Following these steps, we combine both analytic and numeric approaches to elastic fault modeling for analysis of the San Andreas Fault system.

## 3. Modeling the San Andreas Fault Zone

[10] We apply our semianalytic model (Appendix A) to the geometrically complex fault setting of the SAF system. After digitizing the major fault strands along the SAF system from geologic maps [Jennings, 1994] into over 400 elements, we group the elements into 18 fault segments spatially consistent with previous geologic and geodetic studies (Figure 1). Fault segments include the following regions: (1) Imperial, (2) Brawley (defined primarily by seismicity [Hill *et al.*, 1975] rather than by mapped surface trace), (3) Coachella Valley-San Bernardino Mountains, (4) Borrego (includes Superstition Hills and Coyote Creek regions), (5) Anza-San Jacinto (includes San Bernardino Valley), (6) Mojave, (7) Carrizo, (8) Cholame, (9) Parkfield Transition, (10) San Andreas creeping, (11) Santa Cruz Mountains-San Andreas Peninsula, (12) San Andreas North Coast, (13) South Central Calaveras, (14) North Calaveras-Concord, (15) Green Valley-Bartlett Springs, (16) Hayward, (17) Rodgers Creek, and (18) Maacama. The fault system is rotated about its pole of deformation ( $52^\circ\text{N}$ ,  $287^\circ\text{W}$ ) into a new coordinate system [Wdowinski *et al.*, 2001], and fault segments are embedded in a 1-km grid of 2048 elements along the SAF system and 1024 elements across the system (2048 across including the image). We assume that the system is loaded by stresses extending far from the locked portion of the fault and that locking depth and slip rate remain constant along each fault segment.

[11] Each of the 18 SAF segments is assigned a deep slip rate based on geodetic measurements, geologic offsets, and plate reconstructions [WGCEP, 1995, 1999]. In some cases, slip rates (Table 1) were adjusted ( $\pm 5$  mm/yr on

average) in order to satisfy an assumed far-field plate velocity of 40 mm/yr. This constant rate simplifies the model and, as we show below, it has little impact on the near-field velocity, strain rate, and Coulomb stress accumulation rate. Moreover, it provides a remarkably good fit to the geodetic

data, except in the Eastern California Shear Zone, where misfit is expected due to omission of faults in this area. Because slip estimates remain uncertain for the Maacama and Bartlett Springs segments, we assume that these segments slip at the same rates as their southern extensions, the Rodgers Creek and Green Valley faults, respectively.

[12] After assigning these a priori deep slip rates, we estimate lower locking depth for each of the 18 fault segments using a least squares fit to 1099 GPS-derived horizontal velocities. Geodetic data for the southern SAF region, acquired between 1970 and 1997, were provided by the Crustal Deformation Working Group of the Southern California Earthquake Center (SCEC) (D. Agnew, SCEC, Horizontal deformation velocity map version 3.0, personal communication, 2002) GPS velocities for the Calaveras-Hayward region were provided by the U.S. Geological Survey, Stanford University, and the University of California, Berkeley and reflect two data sets, one of campaign measurements (1993–1999) and one of BARD network continuous measurements. Data used to model the northern region of the SAF system were obtained from *Freyemeuller et al.* [1999] and represent campaign measurements from 1991 to 1995. These four geodetic data sets combine to a total of 1099 horizontal velocity vectors spanning the entire San Andreas Fault zone (Figure 2a).

#### 4. Geodetic Inversion

[13] The relationship between surface velocity and locking depth is nonlinear, thus we estimate the unknown depths of the 18 locked fault segments using an iterative, least squares approach based on the Gauss-Newton method. We solve the system of equations  $V_{gps}(x, y) = V_m(x, y, \mathbf{d})$ , where  $V_{gps}$  is the geodetic velocity measurement,  $V_m$  is the modeled velocity, and  $\mathbf{d}$  is the set of locking depth parameters that minimize the weighted residual misfit  $\chi^2$ . The data misfit is

$$V_{res}^i = \frac{V_{gps}^i - V_m^i}{\sigma^i} \quad (1)$$

$$\chi^2 = \frac{1}{N} \sum_{i=1}^N (V_{res}^i)^2 \quad (2)$$

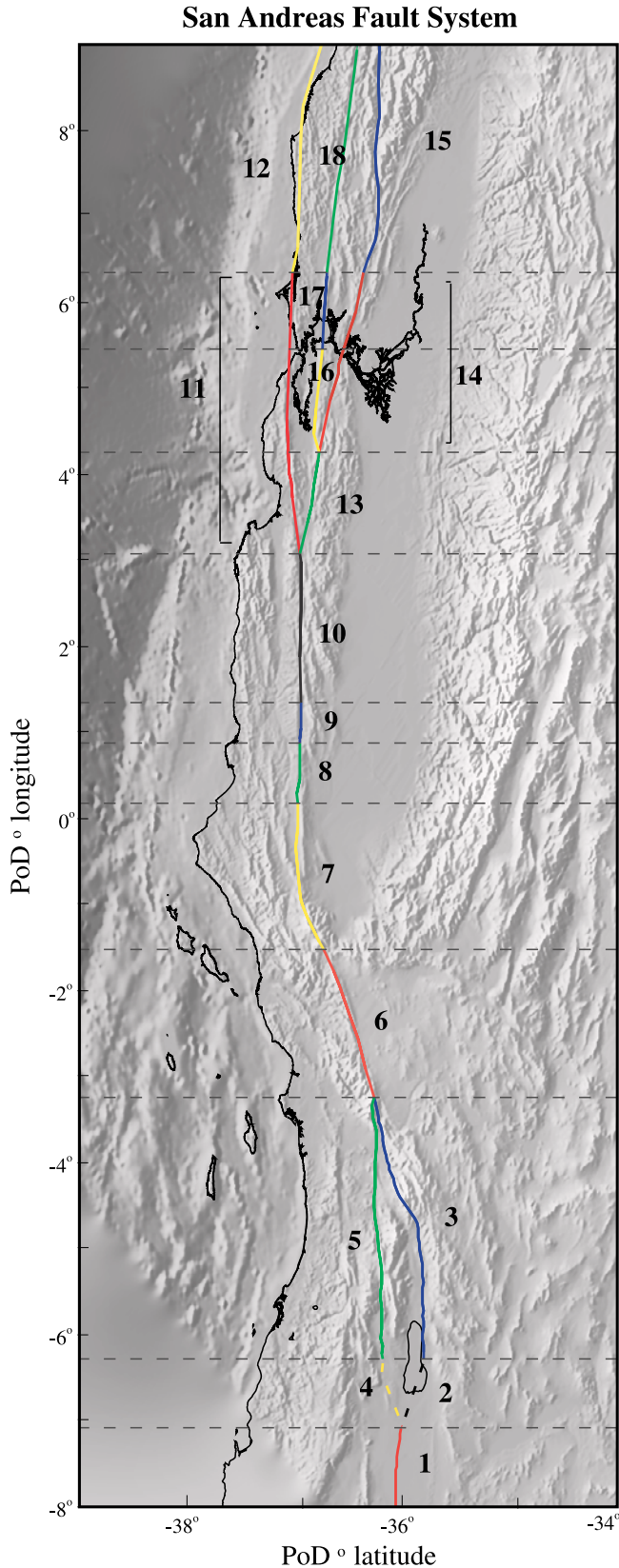


**Figure 1.** (opposite) San Andreas Fault system segment locations in the pole of deformation (PoD) coordinate system over shaded regional topography. Fault segments coinciding with Table 1 are (1) Imperial, (2) Brawley, (3) Coachella Valley-San Bernardino Mountains, (4) Borrego, (5) Anza-San Jacinto, (6) Mojave, (7) Carrizo, (8) Cholame, (9) Parkfield Transition, (10) San Andreas creeping, (11) Santa Cruz Mountains-San Andreas Peninsula, (12) SAF North Coast, (13) South Central Calaveras, (14) North Calaveras-Concord, (15) Green Valley-Bartlett Springs, (16) Hayward, (17) Rodgers Creek, and (18) Maacama. We use the pole of deformation (PoD) of *Wdowinski et al.* [2001] (52°N, 287°W) and note that the longitude axis has been shifted in order to place 0° in the center of the grid. Dashed lines represent horizontal corridor sections, bounded by fault segments, constrained to total 40 mm/yr.

**Table 1.** San Andreas Fault System Parameters and Results

Segment	Name	Slip, <sup>a</sup> mm/yr	Locking Depth, km	$\sigma$ , <sup>b</sup> km	Coulomb Stress, MPa/100 years	Moment Rate, N m/100 years per km $\times 10^{14}$	$\tau_r$ , <sup>a</sup> years
1	Imperial	40	5.9	1.20	10.0	7.1	40
2	Brawley Seismic Zone	36	6.3	1.30	8.5	6.8	24
3	Coachella-San Bernardino Mountains	28	22.6	1.70	1.7	19.0	146
4	Borrogo	4	2.0	7.70	0.5	0.2	175
5	Anza-San Jacinto	12	13.1	2.30	1.7	4.7	83
6	Mojave	40	26.0	1.70	0.6	31.2	150
7	Carrizo	40	25.2	2.60	1.6	30.2	206
8	Cholame	40	12.7	2.40	4.0	15.2	140
9	Parkfield Transition	40	14.5	2.90	4.0	17.4	25
10	San Andreas Creeping	40	1.3	0.20	n/a	1.6	n/a
11	Santa Cruz-Peninsula	21	9.3	0.60	3.2	5.9	401
12	San Andreas North Coast	25	19.4	2.10	2.3	14.6	759
13	South-Central Calaveras	19	1.6	0.20	12.5	0.9	75
14	North Calaveras-Concord	7	13.7	4.60	1.1	2.9	701
15	Green Valley-Bartlett Springs	5	9.1	8.40	1.2	1.4	230
16	Hayward	12	15.7	3.70	1.5	5.7	525
17	Rodgers Creek	12	18.9	6.70	1.1	6.8	286
18	Maacama	10	12.3	4.30	1.7	3.7	220

<sup>a</sup>WGCEP [1995, 1999] and WGNCEP [1996].

<sup>b</sup>Locking depth uncertainty.

where  $\sigma^i$  is the uncertainty estimate of the  $i$ th geodetic velocity measurement and  $N$  is the number of geodetic observations. Uncertainties in each measurement are used to form the diagonal covariance matrix of the data.

[14] The modeled velocity,  $V_m$ , is expanded in a Taylor series about an initial locking depth,  $\mathbf{d}$

$$V_m[\mathbf{d} + \Delta] = V_m[\mathbf{d}] + \sum_{j=1}^M \Delta_j \frac{\partial V_m}{\partial d_j} + \dots \quad (3)$$

where  $\Delta_j$  is a small perturbation to the  $j$ th depth parameter. Partial derivatives are computed analytically using the preintegrated body force solution (Appendix A). Because  $V_m[\mathbf{d} + \Delta]$  is an approximation to the observed velocity,  $V_{gps}$ , the residual velocity may be expressed as the depth perturbation  $\Delta$  times the matrix of partial derivatives  $\delta\mathbf{V}_m$

$$V_{res} = \delta\mathbf{V}_m \Delta. \quad (4)$$

The model perturbation is then calculated using the standard weighted least squares approach

$$\Delta = (\delta\mathbf{V}_m^T \mathbf{C}^{-1} \delta\mathbf{V}_m)^{-1} \delta\mathbf{V}_m^T \mathbf{C}^{-1} V_{res} \quad (5)$$

where  $\mathbf{C}$  is the diagonal covariance matrix of measurement uncertainties. Because of the nonlinear aspects of the inversion, a step length damping scheme is used for each iteration,  $k$ ,

$$d_\gamma^k = d^{k-1} + \gamma \Delta \quad 0 < \gamma < 1 \quad (6)$$

where  $\gamma$  is the damping parameter [Parker, 1994]. Damping parameter  $\gamma$  is chosen such that

$$\chi^2[m_\gamma] = \chi^2[m_k] - 2\gamma\chi^2[m_k] + o \|\gamma\Delta\| \quad (7)$$

will guarantee a smaller misfit than  $\chi^2[m_k]$ . The best fit is obtained by cautiously repeating this algorithm until all 18 locking depth solution parameters converge. Uncertainties

in estimated locking depths are determined from the covariance matrix of the final iteration.

## 5. Results

### 5.1. Horizontal Motion and Locking Depth

[15] Our locking depth inversion involves 26 free parameters: two unknown velocity components for each of the four GPS networks and 18 locking depths (Figures 1 and 2). The unknown velocity component for each of the GPS data sets is estimated by removing the mean misfit from a starting model (uniform locking depth of 10 km). The initial RMS misfit with respect to the starting model is 5.31 mm/yr (unweighted). After 10 iterations, the RMS misfit improves to 2.43 mm/yr (Figure 2). Comparisons between GPS data and fault-parallel modeled velocities for twelve fault corridors are shown in Figure 2b. Each model profile is acquired along a single fault-perpendicular trace, while the geodetic measurements are binned within the fault corridors and projected onto the perpendicular trace, thus some of the scatter is due to projection of the data onto a common profile.

[16] Locking depth inversion results (Table 1) are primarily dependent on data acquired near the fault trace. Uncertainties in these estimates ( $1\sigma$  standard deviation) are relatively low in the southern portion of the SAF system where there is a high density of GPS stations. In contrast, uncertainties are much higher along the northern segments where there is a relatively low density of GPS stations. Our depth solutions are generally consistent with previously published locking depths and distributions of seismicity [Savage, 1990; Johnson et al., 1994; Feigl et al., 1993; Freymueller et al., 1999]. Again, we emphasize that these are apparent locking depths since we have not included the viscoelastic response of the earth to intermittent earthquakes [Thatcher, 1983]. A more detailed discussion of model characteristics and GPS agreement for each of the 18 fault segments is provided in Appendix B.

### 5.2. Far-Field Constraint: 40 mm/yr

[17] Because we are primarily interested in stress behavior close to the fault, the magnitude of the far-field velocity is

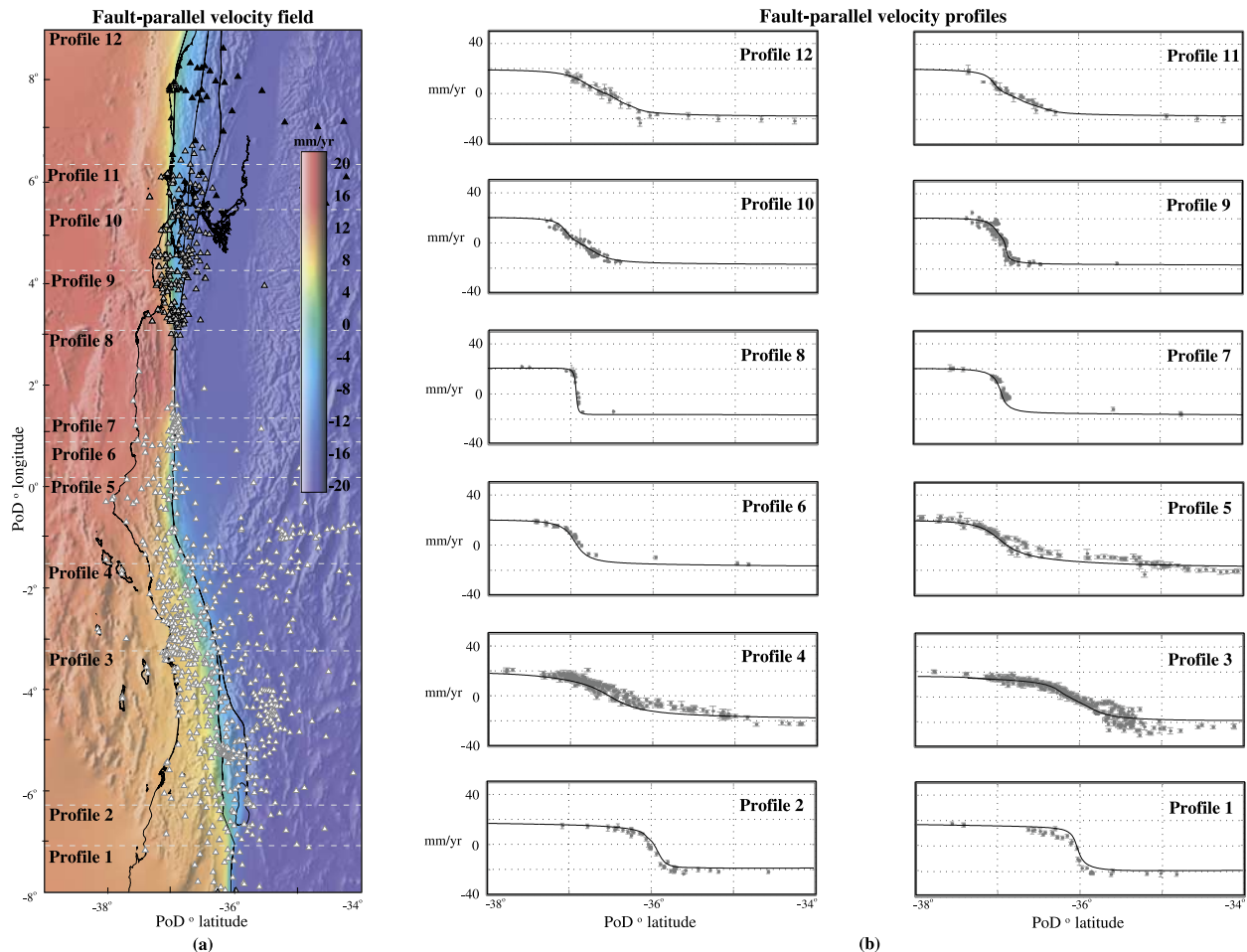


**Figure 2.** (a) Fault-parallel velocity map of best fitting model with shaded topography. Triangles represent GPS station locations used in locking depth analysis. White triangles represent SCEC locations, gray triangles represent the University of California Berkeley-Stanford-USGS stations (two sets), and black triangles represent stations of *Freymueller et al.* [1999]. Dashed lines represent horizontal fault corridor sections of model profiles of Figure 2b. (b) Modeled velocity profiles acquired across the center of each fault corridor with GPS velocities projected onto profile for visual comparison. (Note that the RMS differences between model and data were evaluated at actual GPS locations.)

not the most critical parameter in our analysis. Nevertheless, we attempt to justify the usage of a single far-field rate of 40 mm/yr for the entire SAF system. The full North America-Pacific plate motion is approximately 46 mm/yr [DeMets et al., 1990, 1994]. While the San Andreas Fault system accommodates the majority of deformation occurring between the two plates, substantial regions of deformation also exist far from the SAF system [Minster and Jordan, 1987; Ward, 1990]. These regions include the Eastern California Shear Zone, the Sierra Nevada-Great Basin shear zone, the Garlock fault zone, the Owens Valley Faults zone and the San Jacinto, Whittier-Elsinore, Newport-Inglewood, Palos Verdes, and San Clemente faults. Partitioning details of the total slip rate remain uncertain. The *WGCEP* [1995, 1999] propose a total slip rate of 36–50 mm/yr along the northern portion of the San Andreas Fault system and a rate of 35 mm/yr along the southern portion of the San Andreas Fault system. In this analysis, we adopt a constant far-field velocity of 40 mm/yr for both northern and southern portions of the SAF system. Our results, using realistic fault geometry and variable locking depth, provide an adequate fit to all of

the data (Figure 2b), especially close to the fault zones where we wish to calculate stress accumulation. The far-field regions of the extreme southern and northern SAF system are underestimated by our model (Figure 2b, profiles 1–4, 11, 12), while the middle portions of the system are well matched in the far field (Figure 2b, profiles 6, 7, 9). There is significant misfit on the eastern sides of profiles 3, 4, and 5, which reflect both coseismic and interseismic shear in the Mojave desert. The apparent locking depth along these profiles may be artificially high in order to minimize the misfit in the Eastern California Shear Zone. Nevertheless, we have found that increasing the far-field velocity to 45 mm/yr, for example, does not significantly improve the fit to the GPS data and yields long-term slip rates that are inconsistent with published estimates [WGCEP, 1995, 1999]. Overall, the match to the GPS data is quite good considering the simplicity of the model.

### 5.3. Vertical Motion

[18] An intuitive yet important aspect of our 3-D model is the vertical component of deformation (Figure 3), driven

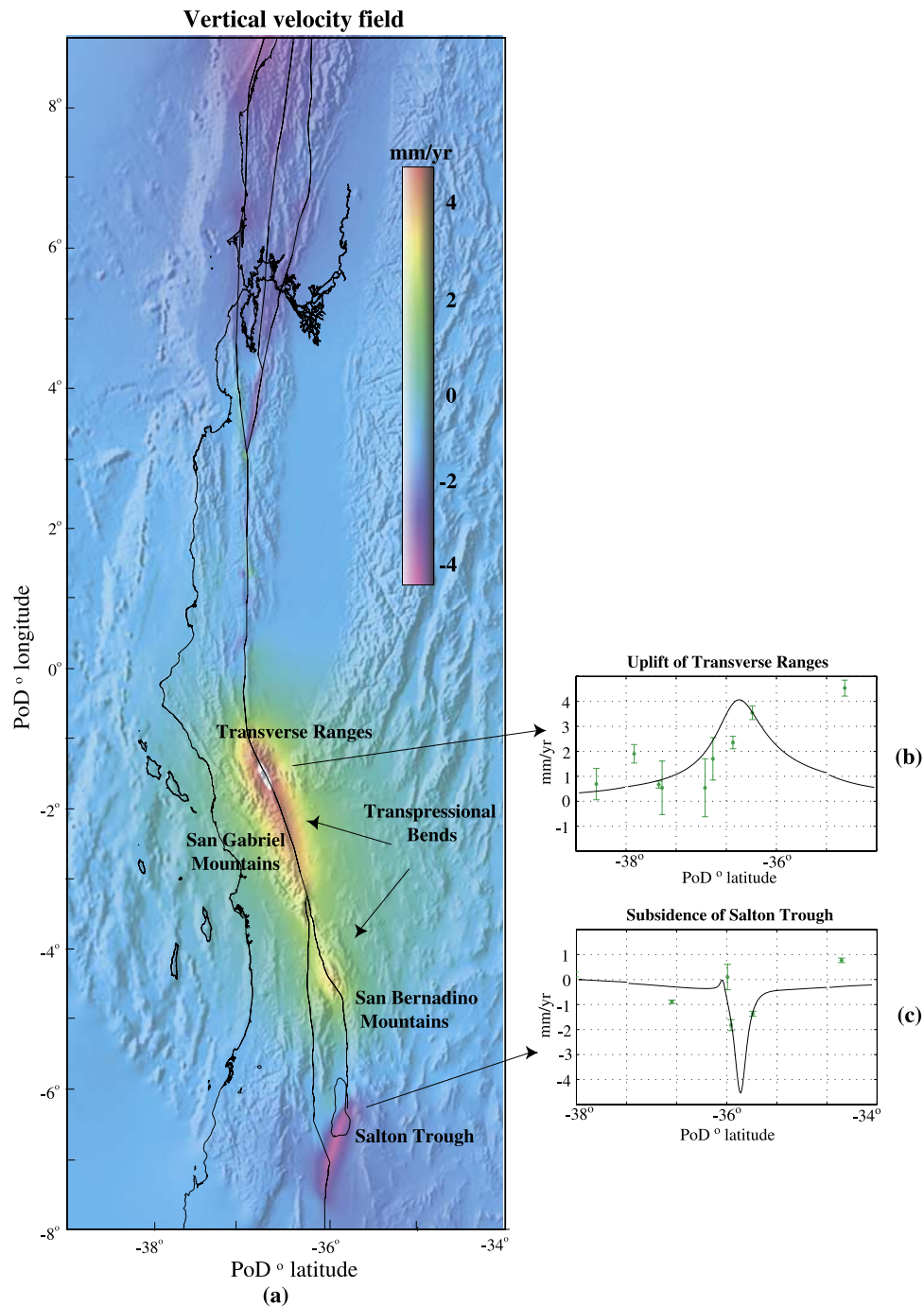


**Figure 3.** (a) Vertical velocity model with shaded topography (positive uplift and negative subsidence). Transpressional bends [Atwater, 1998] are shown, along with corresponding topographical features of the Transverse Ranges, San Gabriel, and San Bernardino Mountains. (b) Profile of vertical velocity model across uplifting region the Big Bend and sampled SCIGN vertical velocities. (c) Profile of vertical velocity model across subsiding region of Salton Trough and sampled SCIGN vertical velocities.

entirely by horizontal force. Moreover, because the model parameters are constrained using only horizontal GPS velocity measurements, resulting vertical deformation can be checked against both geologically inferred and geodetically measured vertical rates. For simplicity, our model does not include the effects of topography. To develop the model, we assume that the far-field driving stress is always parallel to the relative plate motion vector. Because the fault segments are not always parallel to this driving stress, hori-

zontal motion on free slipping fault planes has both a fault-parallel and fault-perpendicular component. It is the fault-perpendicular component that drives most of the vertical deformation. For example, in the Big Bend area (Figure 3a) where the fault trace is rotated counterclockwise with respect to the far-field stress vector, the fault-normal stress is compressional; this results in uplift rates of 2–4 mm/yr in this region. Fault-normal extensional stress occurs where the strike of the fault is rotated clockwise with respect to the

far-field stress vector. This occurs in regions such as the Salton Trough, where our model predicts subsidence rates of 1–4 mm/yr.

[19] Our predicted vertical motion is in good agreement with recent geological activity. Approximately 8 Myr ago, the North American-Pacific plate boundary began to acquire a transpressional, or shortening, component as its relative velocity vector rotated clockwise with respect to the strike of the present SAF. Approximately 5 Myr ago, the Pacific plate captured Southern California and Baja California [Atwater, 1998], initiating the strike-slip plate boundary of the San Andreas Fault system. As a result, the current geometry of the SAF system has a prominent bend between Fort Tejon and the San Geronio Pass where the fault orientation has rotated from its conventional N40°W strike to a N70°W orientation [Jones, 1988]. This transpressional bend has produced the San Bernardino Mountains along with numerous thrust faults and the east-west trending Transverse Ranges. The Garlock fault and its left-lateral motion is a response to such transpressional behavior [Atwater, 1998].

[20] Regions of prominent uplift produced by our model coincide with present topographic features such as the Transverse Ranges, the San Gabriel, and the San Bernardino Mountains (Figure 3a). We find a maximum uplift rate of 4.5 mm/yr occurring where the Garlock fault intersects the main San Andreas Fault strand. We do not include the effects of the east-west striking Garlock fault into this analysis, but suspect that slip along the Garlock fault would reduce the fault-normal compressional stress and thus reduce the uplift rate. Williams and Richardson [1991] report similar uplift rates of up to 3.5 mm/yr for this area from their 3-D kinematic finite element model. Further south, the uplifting region of the Carrizo-Mojave segment gradually decreases (3 mm/yr), following the San Andreas Fault trace and the San Gabriel Mountains. Geologic estimates of late Quaternary uplift rate for the southern and central San Gabriel Mountains range from 3 to 10 mm/yr [Brown, 1991]. The intersection of the San Jacinto and San Bernardino-Coachella segments corresponds to a local minimum in the uplift rate. Even further south, our model predicts a local maximum uplift rate of 2 mm/yr at the San Bernardino Mountains. Yule and Sieh [1997] estimate a minimum uplift rate of 2 mm/yr just south of the San Bernardino Mountains based on excavation measurements near the San Geronio pass.

[21] Another primary feature of our vertical model is the subsiding region of the Salton Trough (Figure 3a). Although the geologic extension of the Salton Trough is well mapped, there is no consensus on how the strike-slip motion on the Imperial Fault is transferred to the southern San Andreas along the Brawley Seismic zone. This extensional step over is likely to form a rifting site that will eventually evolve into a spreading center similar to that of the Gulf of California [Lomnitz *et al.*, 1970; Elders *et al.*, 1972; Johnson and Hadley, 1976; Larsen and Reilinger, 1991]. Leveling surveys of this region reveal a subsidence estimate of 3 mm/yr [Larsen and Reilinger, 1991]. Our model predicts approximately 4–8 mm/yr of localized subsidence in the Brawley-Imperial zone, located just south of the Salton Sea. Johnson *et al.* [1994] find a similar dilatational pattern in the Salton Trough from a kinematic

model of slip transfer between the southern San Andreas Fault and the Imperial Fault.

[22] Vertical deformation predicted by our model is also in general agreement with geodetic measurements. Historically, vertical uplift has been estimated from repeated leveling surveys, and the interpretation of these results has often been speculative due to the low signal-to-noise ratio [Stein, 1987; Craymer and Vanicek, 1989]. More recent surveys, using methods such as VLBI, SLR, and GPS, have significantly improved the acquisition and accuracy of vertical measurements [Williams and Richardson, 1991]. While such observations along the San Andreas Fault are spatially restricted and generally accompany large uncertainties, it is conceivable that these measurements may play a role in refining our understanding of the rheological structure of the Earth's crust [Pollitz *et al.*, 2001]. A preliminary comparison of continuous geodetic vertical measurements from the Southern California Integrated GPS Network (SCIGN) (R. Nikolaidis, personal communication, 2002) from the Big Bend and Salton Trough shows reasonable agreement with the model predictions (Figures 3b and 3c). Note that the vertical rates inferred from the GPS data have relatively large uncertainties (up to  $\pm 2$  mm/yr).

#### 5.4. Static Coulomb Stress and Seismic Moment Accumulation

[23] Deep slip along the San Andreas Fault system gives rise to stress accumulation on the upper locked portions of the fault network. After a period of time, often described as the recurrence interval, these stresses are released by seismic events. The rate of stress accumulation and earthquake recurrence interval can be used to estimate the average stress drops during major seismic events. Similarly, the seismic moment accumulation rate per unit length of a fault [Ward, 1994; Savage and Simpson, 1997], combined with recurrence intervals, can provide an estimate of the seismic “potential” of a fault segment. Our model can be used to estimate these quantities in the form of Coulomb stress and seismic moment accumulation rate.

[24] To calculate Coulomb stress, we follow the approach of King *et al.* [1994] and Simpson and Reasenber [1994] [also see Stein and Lisowski, 1983; Oppenheimer *et al.*, 1988; Hudnut *et al.*, 1989; Harris and Simpson, 1992]. The Coulomb failure criterion is

$$\sigma_f = \tau - \mu_f \sigma_n \quad (8)$$

where  $\sigma_n$  and  $\tau$  are the normal and shear stresses on a failure plane and  $\mu_f$  is the effective coefficient of friction. Our semianalytic model (Appendix A) provides the 3-D vector displacement field from which we compute the stress tensor. For a vertical fault plane with strike-slip motion, only the horizontal stress components are needed:  $\sigma_{xx}$ ,  $\sigma_{yy}$ ,  $\tau_{xy}$ . The normal and shear stresses resolved on the fault plane are

$$\begin{aligned} \sigma_n &= \sigma_{xx} \sin^2 \theta - 2\sigma_{xy} \sin \theta \cos \theta + \sigma_{yy} \cos^2 \theta \\ \tau &= \frac{1}{2} (\sigma_{yy} - \sigma_{xx}) \sin 2\theta + \tau_{xy} \cos 2\theta \end{aligned} \quad (9)$$

where  $\theta$  is the orientation of the fault plane with respect to the  $x$  axis. Right-lateral shear stress and extension are assumed to be positive.

[25] Our objective is to calculate Coulomb stress accumulation rate on each of the 18 fault segments. Coulomb stress is zero at the surface and becomes singular at the locking depth as  $d_j/(d_j^2 - z^2)$ . Each segment has a different locking depth  $d_j$ , so to avoid the singularity, we calculate the representative Coulomb stress accumulation rate at 1/2 of the local locking depth [King *et al.*, 1994]. This calculation is performed on a fault segment by fault segment basis, thus only the local fault contributes to the final Coulomb stress result. For the SAF system, the largest angular deviation of a local segment from the average slip direction is  $\sim 18^\circ$ , thus the normal stress contribution to the total Coulomb stress calculation is generally less than 10% (equation 8). Therefore the exact value of the effective coefficient of friction is not important. Choosing  $\mu_f$  to be 0.6, our model predicts Coulomb stress accumulation rates ranging from 0.5 to 12.5 MPa/100 years (Figure 4a) for the segments of the SAF system. Average values of Coulomb stress accumulation along each segment are listed in Table 1. Because stress drops during major earthquakes rarely exceed 10 MPa, this calculation may provide an upper bound on the expected recurrence interval on each of the 18 fault segments as discussed below.

[26] In addition to calculating the stress accumulation rate, our model provides a straightforward estimate of seismic moment accumulation rate per unit length of fault,  $l$ . Moment accumulation rate  $\dot{M}_j$  depends on locking depth  $d_j$ , slip rate  $v_j$ , and the rock shear modulus  $\mu$

$$\frac{\dot{M}_j}{l} = \mu d_j v_j. \quad (10)$$

Moment accumulation rate is often calculated from observed rates of surface strain accumulation [WGCEP, 1995, 1999; Ward, 1994; Savage and Simpson, 1997] and typically evaluated for a locking depth of 11–12 km [WGCEP, 1995; WGNCEP, 1996]. For this analysis, we use our locking depth estimates (Table 1) and equation 10 to calculate seismic moment accumulation rate per unit length for each fault segment of the SAF system, shown in Figure 4b (Table 1). As expected, high rates of moment accumulation ( $31.2 \times 10^{14}$  N m/100 year per km) occur where the locking depth is greatest, such as along the Big Bend area (segment 6 of the SAF), and low rates ( $1.6 \times 10^{14}$  N m/100 year per km) occur where the fault creeps from nearly top to bottom (SAF creeping segment) of the SAF system.

## 6. Discussion

[27] The main parameters affecting Coulomb stress accumulation are locking depth, slip rate, and fault strike. Coulomb stress accumulates fastest in regions of shallow locking depth and high slip rate (Figure 4a). It is also slightly enhanced or reduced if the fault orientation is releasing or restraining, respectively. Moreover, there is a correlation between locking depth and fault orientation suggesting that tectonically induced normal stress has an important influence on depth-averaged fault strength. *Wdowinski et al.* [2001] observe similar regions of high strain

rate within the creeping Parkfield segment, the Cholame segment, the lower Coachella Valley segment, and along the Imperial segment where the relative plate motion vector is well aligned with fault strike. In addition, they also find diffuse regions of lower magnitude strain rate corresponding to the lower Carrizo segment and along the entire Mojave segment.

[28] We also note an intriguing correlation between regions of high Coulomb stress accumulation and nucleation sites of large historical earthquakes along the San Andreas Fault system. Epicenters of such earthquakes occurring between 1796 and 2000 with magnitudes greater than 5.0 (contributed primarily by *Ellsworth* [1990]) are shown in Figure 4a. Moderate earthquakes ( $M = 5.0-7.0$ ) are frequently found to occur in regions such as the Imperial Valley, San Jacinto-San Bernardino junction, Central San Andreas, Santa Cruz-Peninsula, and Southern Calaveras-Hayward faults. However, large events such as the Fort Tejon earthquake of 1857 ( $M = 8.2$ ), the Great San Francisco earthquake of 1906 ( $M = 8.25$ ), the Imperial Valley event of 1940 ( $M = 7.1$ ), and the more recent Loma Prieta event of 1989 ( $M = 7.1$ ) have all nucleated in zones of high Coulomb stress accumulation. The San Jacinto-San Bernardino region, where the two major fault strands converge, is particularly interesting because it has moderate Coulomb stress accumulation and has also experienced numerous magnitude 6.0–7.0 events between 1858 and 1923 (San Bernardino, Wrightwood, San Jacinto, and Lytle Creek).

### 6.1. Coulomb Stress and Fault Creep

[29] Coulomb stress accumulation rate is also positively correlated with shallow fault creep. Faults are relatively weak at shallow depth because the normal stress due to overburden pressure is low. Thus creep may occur on segments where most of the stress is supported at shallow depths [Savage and Lisowski, 1993]. Our model demonstrates such behavior in the Imperial region, the Brawley seismic zone, and the Calaveras segment, where shallow creep has been known to occur [Genrich and Bock, 1997; Bakun, 1999; Lyons *et al.*, 2002]. We also note that while the Parkfield segment is found to have moderate locking depth (14 km) in our analysis, it also demonstrates high shallow stress accumulation. As discussed above, this is due to “straight” fault geometry and the fact that there is no partitioning of stress between subparallel fault strands. We do not find a significant correlation of high Coulomb stress with the Maacama, Hayward, and Concord-Green Valley segments (also known to have contributions of shallow creep [WGNCEP, 1996; Burgmann *et al.*, 2000; Savage and Lisowski, 1993]), which we attribute to our larger locking depth estimates.

### 6.2. Moment Accumulation Rate

[30] As described above, our model is also used to estimate seismic moment accumulation rate per unit length along each fault segment (Figure 4b). These rates can be compared with stress accumulation rate and recurrence interval to establish seismic hazard [WGCEP, 1995, 1999; WGNCEP, 1996]. In our analysis, fault segments with high seismic moment accumulation rate are associated with deep locking depth, while faults with shallow locking depth have lower seismic moment accumulation rate and corresponding

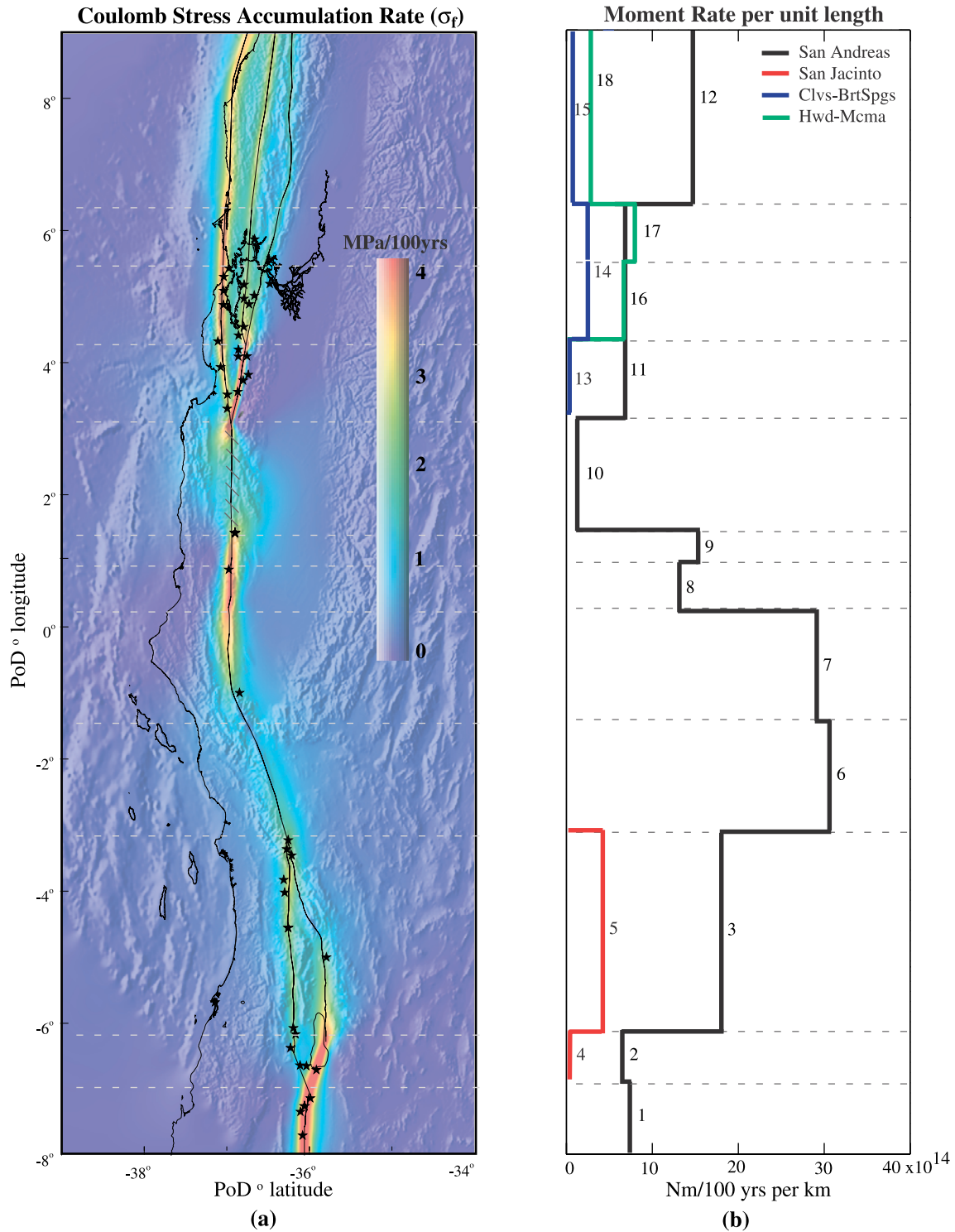


**Figure 4.** (a) Coulomb stress accumulation of the SAF system in MPa/100 years with shaded topography. Color scale is saturated at 4 MPa/100 years. Locations of significant earthquakes occurring on the San Andreas Fault system from 1769 to 2000 (primarily contributed by *Ellsworth* [1990]) are shown as black stars. Segment 10 (creeping SAF) was not included in the stress calculation and is marked with hash marks. Dashed lines represent horizontal fault corridor sections used in Figures 1 and 2. (b) Seismic moment accumulation per unit length of modeled segments in N m/100 years per length, labeled by segment numbers. The black solid line represents moment rate along the primary San Andreas strand (segments 1–3, 6–12). The red solid line represents moment rate along the San Jacinto strand (segments 4 and 5). The blue solid line represents moment rate of the Calaveras-Bartlett Springs strand (segments 13–15). The green solid line represents moment rate along the Hayward-Maacama strand (segments 16–18). Dashed lines represent horizontal fault corridor sections used in Figures 1 and 2.

hazard potential [Burgmann *et al.*, 2000]. In general, we find that the main San Andreas Fault strand (segments 1–3, 6–12) accumulates most of the seismic moment (Figure 4b, black line), while subfaults (segments 4–5, 13–18) tend to accumulate less seismic moment (Figure 4b, red, green, and blue lines). One exception is the Hayward and Rodgers Creek segments (green) where moment accumulation rate is comparable to the adjacent San Andreas segment. The *WGCEP* [1999] similarly recognizes the Hayward-Rodgers Creek Faults as regions of elevated seismic potential.

[31] Comparing the accumulation rates of both seismic moment and Coulomb stress, we find an inverse correlation, primarily due to the locking depth proportionality of each calculation. Seismic moment is directly proportional to locking depth, whereas Coulomb stress is approximately inversely proportional to locking depth. For example, more shallowly locked regions such as the Imperial Fault, the Brawley Seismic Zone, and the Calaveras Fault segments have high Coulomb stress accumulation rate and low seismic moment accumulation rate. Conversely, regions of the Mojave and San Bernardino-Coachella Valley segments have high seismic moment accumulation rate and low Coulomb stress accumulation rate. These areas have deep locking depths, greater than 20 km, which tend to absorb seismic moment while diluting accumulated stress. Other areas of interest include the Cholame and Parkfield segments with moderate seismic moment accumulation but high Coulomb stress accumulation rate. The Cholame and Parkfield segments have moderate locking depths (12–14 km) and produce expected amounts of seismic moment rate. However, these segments have nearly zero azimuthal angle with respect to driving stress vector and also support the entire motion of the SAF in this region, giving rise to high Coulomb stress accumulation.

### 6.3. Coulomb Stress and Earthquake Frequency

[32] Average recurrence interval provides a more quantitative association between earthquake hazard potential (i.e., stress drop) and Coulomb stress accumulation rate. Estimates of recurrence interval,  $\tau_r$ , compiled by the *WGCEP* [1995, 1999] and the *WGNCEP* [1999], are listed in Table 1 for each of the 18 fault segments. Assuming that all accumulated stress is released during major earthquakes, and given that earthquake stress drops are typically less than 10 MPa, an inverse correlation should exist between recurrence interval and Coulomb stress accumulation rate (Figure 5). The data for segments of the SAF system clearly demonstrate this inverse correlation, lying primarily within the margins of 1–10 MPa stress drop events with one primary exception; Segment 11 (Santa Cruz-Peninsula) has an exceptionally long recurrence interval, which may be due to the San Gregorio fault to the west [WGCEP, 1999]. The correlation is particularly good for remaining segments, implying that over a characteristic time period, these regions accumulate sufficient amounts of tectonic stress that result in large periodic earthquakes of 1–10 MPa stress drops.

[33] Heat flow measurements suggest that the San Andreas Fault may not support shear stresses greater than 10 MPa [Lachenbruch and Sass, 1988], implying that the SAF is much weaker than predictions based on simple rock friction [Byerlee, 1978]. Our estimates of Coulomb stress accumulation over realistic seismic intervals fall well within

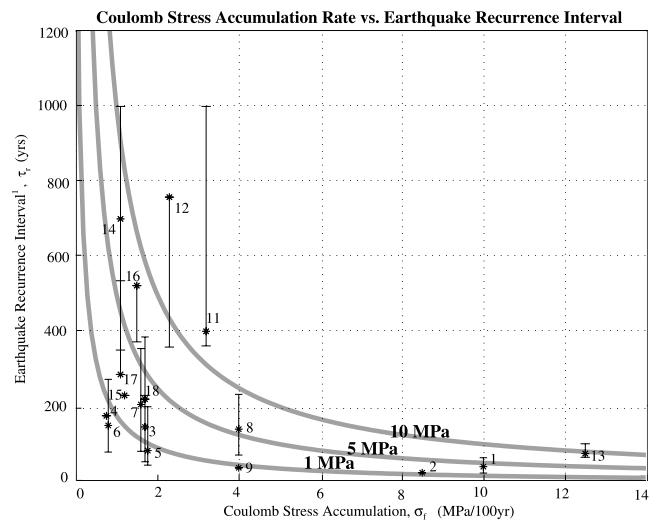


**Figure 5.** Published recurrence intervals of the SAF system,  $\tau_r$  [WGCEP, 1995, 1999; WGNCEP, 1996], versus Coulomb stress accumulation rate,  $\sigma_f$ , (Table 1). Segment 4 was acquired from Peterson *et al.* [1996]. Error bars were estimated by combining published results and uncertainty estimates. Segment numbers are labeled according to Table 1. Three characteristic stress drops are shown as thick gray lines, derived from the equation,  $\tau_r = \Delta\sigma/\sigma_f$  reflecting constant stress drops of  $\Delta\sigma = 1, 5,$  and  $10$  MPa.

this limit. However, it is still possible that typical earthquake stress drop is only a fraction of the total tectonic stress if some of the heat is transported by hydrothermal processes.

## 7. Conclusion

[34] In summary, we have developed and tested a semi-analytical model for the 3-D response of an elastic half-space to an arbitrary distribution of single-couple body forces. For a vertical fault, 2-D convolutions are performed in the Fourier transform domain, and thus displacement, strain, and stress due to a complicated fault trace can be computed very quickly. Using the correspondence principle, the method can be easily extended to a viscoelastic half-space without unreasonable computational burden.

[35] We have used this method to estimate the velocity and stress accumulation rate along the entire San Andreas Fault system. Average slip rates along individual fault strands are based on long-term geological rates as well as recent geodetic measurements. The far-field slip rate is set to the best long-term average for the entire SAF system of 40 mm/yr. Horizontal components of GPS-derived velocities (1099 rates and uncertainties) are used to solve for variations in apparent locking depth for 18 primary segments. Locking depths vary between 1.3 km and 26.0 km. The horizontally driven model also predicts vertical deformation rates consistent with geological estimates and geodetic measurements. From the analysis of shear and normal stress near the major fault strands, we find the following:

[36] 1. Coulomb stress accumulation rate is dependent on slip partitioning and inversely proportional to locking depth. At midseismogenic depths, high Coulomb stress accumu-

lation rate is correlated with shallow fault creep. Low Coulomb stress accumulation occurs along sections where stress is partitioned on multiple strands.

[37] 2. Seismic moment accumulation rate is greatest along deeply locked segments of the SAF system that accommodate the full relative plate motion.

[38] 3. Recurrence intervals of major earthquakes along the San Andreas Fault system are inversely related to Coulomb stress accumulation rate consistent with coseismic stress drops from 1 to 10 MPa.

[39] This steady state model is obviously too simple to explain the complex time-dependent stress evolution of the SAF system and we have ignored several important processes such as postseismic deformation, changes in local pore pressure, and stress perturbations due to nearby earthquakes. Nevertheless, the agreement and predictions of this simple model are encouraging and provide a baseline for the development of more realistic 3-D time-dependent models.

## Appendix A: Analytic 3-D Body Force Model

[40] We wish to calculate the displacement vector  $\mathbf{u}(x, y, z)$  due to a vector body force at depth. This approach is used to describe motion on both curved and discontinuous faults, and is also used to evaluate stress regimes above the upper locking depth. For simplicity, we ignore the effects of Earth's sphericity. We assume a Poisson material, and maintain constant moduli with depth. A major difference between this solution and the *Okada* [1985, 1992] solutions is that we consider deformation due to a vector body force, while the *Okada* solution considers deformation due to a dislocation.

[41] While the following text provides a brief outline of our model formulation, the full derivation and source code of our semianalytic Fourier model can be found at [http://topex.ucsd.edu/body\\_force](http://topex.ucsd.edu/body_force). Our solution is obtained as follows:

[42] 1. Develop three differential equations relating a 3-D vector body force to a 3-D vector displacement. We apply a simple force balance in a homogeneous, isotropic medium and after a series of substitutions for stress, strain, and displacement, we arrive at equation A1, where  $u$ ,  $v$ , and  $w$  are vector displacement components in  $x$ ,  $y$ , and  $z$ ,  $\lambda$  and  $\mu$  are Lamé parameters,  $\rho_j$  are vector body force components:

$$\begin{aligned} \mu \nabla^2 u + (\lambda + \mu) \left[ \frac{\partial^2 u}{\partial x^2} + \frac{\partial^2 v}{\partial y \partial x} + \frac{\partial^2 w}{\partial z \partial x} \right] &= -\rho_x \\ \mu \nabla^2 v + (\lambda + \mu) \left[ \frac{\partial^2 u}{\partial x \partial y} + \frac{\partial^2 v}{\partial y^2} + \frac{\partial^2 w}{\partial z \partial y} \right] &= -\rho_y \\ \mu \nabla^2 w + (\lambda + \mu) \left[ \frac{\partial^2 u}{\partial x \partial z} + \frac{\partial^2 v}{\partial y \partial z} + \frac{\partial^2 w}{\partial z^2} \right] &= -\rho_z \end{aligned} \quad (\text{A1})$$

A vector body force is applied at  $x = y = 0$ ,  $z = a$ . To partially satisfy the boundary condition of zero shear traction at the surface, an image source is also applied at  $x = y = 0$ ,  $z = -a$  [Weertman, 1964]. Equation (A2) describes a point body force at both source and image locations, where  $F$  is a vector force with units of force:

$$\rho(x, y, z) = \mathbf{F} \delta(x) \delta(y) \delta(z - a) + \mathbf{F} \delta(x) \delta(y) \delta(z + a) \quad (\text{A2})$$

[43] 2. Take the 3-D Fourier transform of equations (A1) and (A2) to reduce the partial differential equations to a set of linear algebraic equations.

[44] 3. Invert the linear system of equations to isolate the 3-D displacement vector solution for  $U(\mathbf{k})$ ,  $V(\mathbf{k})$ , and  $W(\mathbf{k})$ .

$$\begin{aligned} \begin{bmatrix} U(\mathbf{k}) \\ V(\mathbf{k}) \\ W(\mathbf{k}) \end{bmatrix} &= \frac{(\lambda + \mu)}{|\mathbf{k}|^4 \mu (\lambda + 2\mu)} \\ &\cdot \begin{bmatrix} (k_y^2 + k_z^2) + \frac{\mu |\mathbf{k}|^2}{(\lambda + \mu)} & -k_y k_x & -k_z k_x \\ -k_x k_y & (k_x^2 + k_z^2) + \frac{\mu |\mathbf{k}|^2}{(\lambda + \mu)} & -k_z k_y \\ -k_x k_z & -k_y k_z & (k_x^2 + k_y^2) + \frac{\mu |\mathbf{k}|^2}{(\lambda + \mu)} \end{bmatrix} \\ &\cdot \frac{(e^{-i2\pi k_z a} + e^{i2\pi k_z a})}{4\pi^2} \begin{bmatrix} F_x \\ F_y \\ F_z \end{bmatrix} \end{aligned} \quad (\text{A3})$$

where  $\mathbf{k} = (k_x, k_y, k_z)$  and  $|\mathbf{k}|^2 = \mathbf{k} \bullet \mathbf{k}$ .

[45] 4. Perform the inverse Fourier transform in the  $z$  direction (depth) by repeated application of the Cauchy residue theorem. We assume  $z$  to be positive upward.

[46] 5. Solve the Boussinesq problem to correct for nonzero normal traction on the half-space. This derivation follows the approach of *Steketee* [1958] where we impose a negative surface traction in an elastic half-space in order to cancel the nonzero traction from the source and image in the elastic full-space.

[47] 6. Integrate the point source Green's function to simulate a fault. For a complex dipping fault, this integration could be done numerically. However, if the faults are assumed to be vertical, the integration can be performed analytically. The body force is applied between the lower depth  $d_1$  (e.g., minus infinity) and the upper depth  $d_2$  (Figure A1). The displacement or stress (derivatives are computed analytically) can be evaluated at any depth  $z$  above  $d_2$ . Note that the full displacement solution is the sum of three terms: a source, an image, and a Boussinesq correction.

$$\begin{aligned} \begin{bmatrix} U(\mathbf{k}) \\ V(\mathbf{k}) \\ W(\mathbf{k}) \end{bmatrix} &= \begin{bmatrix} U_{xs} & U_{ys} & U_{zs} \\ U_{ys} & V_{ys} & V_{zs} \\ U_{zs} & V_{zs} & W_{zs} \end{bmatrix} \begin{bmatrix} F_x \\ F_y \\ F_z \end{bmatrix} + \begin{bmatrix} U_{xi} & U_{yi} & -U_{zi} \\ U_{yi} & V_{yi} & -V_{zi} \\ U_{zi} & V_{zi} & -W_{zi} \end{bmatrix} \\ &\cdot \begin{bmatrix} F_x \\ F_y \\ F_z \end{bmatrix} + \begin{bmatrix} U_B \\ V_B \\ W_B \end{bmatrix} \end{aligned} \quad (\text{A4})$$

[48] The individual elements of the source and image tensors are

$$U_{xx}(\mathbf{k}) = \frac{C}{\beta^2} \left\{ e^{-\beta(z-d_2)} \left[ D + \frac{k_y^2}{|\mathbf{k}|^2} - \frac{k_x^2}{|\mathbf{k}|^2} (1 + \beta(z-d_2)) \right] - e^{-\beta(z-d_1)} \left[ D + \frac{k_y^2}{|\mathbf{k}|^2} - \frac{k_x^2}{|\mathbf{k}|^2} (1 + \beta(z-d_1)) \right] \right\}$$

$$U_{yy}(\mathbf{k}) = -\frac{C}{\beta^2} \frac{k_x k_y}{|\mathbf{k}|^2} \left\{ e^{-\beta(z-d_2)} (2 + \beta(z-d_2)) - e^{-\beta(z-d_1)} (2 + \beta(z-d_1)) \right\}$$

$$U_{zz}(\mathbf{k}) = -i \frac{C}{\beta^2} \frac{k_x}{|\mathbf{k}|} \left\{ e^{-\beta(z-d_2)} (1 + \beta(z-d_2)) - e^{-\beta(z-d_1)} (1 + \beta(z-d_1)) \right\}$$

$$V_{yx}(\mathbf{k}) = \frac{C}{\beta^2} \left\{ e^{-\beta(z-d_2)} \left[ D + \frac{k_x^2}{|\mathbf{k}|^2} - \frac{k_y^2}{|\mathbf{k}|^2} (1 + \beta(z-d_2)) \right] - e^{-\beta(z-d_1)} \left[ D + \frac{k_x^2}{|\mathbf{k}|^2} - \frac{k_y^2}{|\mathbf{k}|^2} (1 + \beta(z-d_1)) \right] \right\}$$

$$V_{zy}(\mathbf{k}) = -i \frac{C}{\beta^2} \frac{k_y}{|\mathbf{k}|} \left\{ e^{-\beta(z-d_2)} (1 + \beta(z-d_2)) - e^{-\beta(z-d_1)} (1 + \beta(z-d_1)) \right\}$$

$$W_{zx}(\mathbf{k}) = \frac{C}{\beta^2} \left\{ e^{-\beta(z-d_2)} [D + 1 + \beta(z-d_2)] - e^{-\beta(z-d_1)} [D + 1 + \beta(z-d_1)] \right\}$$

$$U_{xi}(\mathbf{k}) = \frac{C}{\beta^2} \left\{ e^{\beta(z+d_2)} \left[ D + \frac{k_y^2}{|\mathbf{k}|^2} - \frac{k_x^2}{|\mathbf{k}|^2} (1 - \beta(z+d_2)) \right] - e^{\beta(z+d_1)} \left[ D + \frac{k_y^2}{|\mathbf{k}|^2} - \frac{k_x^2}{|\mathbf{k}|^2} (1 - \beta(z+d_1)) \right] \right\}$$

$$U_{yi}(\mathbf{k}) = -\frac{C}{\beta^2} \frac{k_x k_y}{|\mathbf{k}|^2} \left\{ e^{\beta(z+d_2)} (2 - \beta(z+d_2)) - e^{\beta(z+d_1)} (2 - \beta(z+d_1)) \right\}$$

$$U_{zi}(\mathbf{k}) = i \frac{C}{\beta^2} \frac{k_x}{|\mathbf{k}|} \left\{ e^{\beta(z+d_2)} (1 - \beta(z+d_2)) - e^{\beta(z+d_1)} (1 - \beta(z+d_1)) \right\}$$

$$V_{yi}(\mathbf{k}) = \frac{C}{\beta^2} \left\{ e^{\beta(z+d_2)} \left[ D + \frac{k_x^2}{|\mathbf{k}|^2} - \frac{k_y^2}{|\mathbf{k}|^2} (1 - \beta(z+d_2)) \right] - e^{\beta(z+d_1)} \left[ D + \frac{k_x^2}{|\mathbf{k}|^2} - \frac{k_y^2}{|\mathbf{k}|^2} (1 - \beta(z+d_1)) \right] \right\}$$

$$V_{zi}(\mathbf{k}) = i \frac{C}{\beta^2} \frac{k_y}{|\mathbf{k}|} \left\{ e^{\beta(z+d_2)} (1 - \beta(z+d_2)) - e^{\beta(z+d_1)} (1 - \beta(z+d_1)) \right\}$$

$$W_{zi}(\mathbf{k}) = \frac{C}{\beta^2} \left\{ e^{\beta(z+d_2)} [D + 1 - \beta(z+d_2)] - e^{\beta(z+d_1)} [D + 1 - \beta(z+d_1)] \right\}$$

where

$$C = \frac{(\lambda + \mu)}{4\mu(\lambda + 2\mu)} \quad D = \frac{\lambda + 3\mu}{\lambda + \mu} \quad \alpha = \frac{\lambda + \mu}{\lambda + 2\mu}$$

$$|\mathbf{k}| = \left( k_x^2 + k_y^2 \right)^{1/2} \quad \beta = 2\pi|\mathbf{k}|.$$

[49] The individual elements of the Boussinesq correction are

$$U_B = -i2\pi k_x \frac{1}{2\mu} \frac{\tau_3(\mathbf{k})}{\beta^3} \left[ 1 - \frac{1}{\alpha} - \beta z \right] e^{\beta z}$$

$$V_B = -i2\pi k_y \frac{1}{2\mu} \frac{\tau_3(\mathbf{k})}{\beta^3} \left[ 1 - \frac{1}{\alpha} - \beta z \right] e^{\beta z} \quad (\text{A6})$$

$$W_B = -\frac{1}{2\mu} \frac{\tau_3(\mathbf{k})}{\beta^2} \left[ \frac{1}{\alpha} - \beta z \right] e^{\beta z}$$

where

$$\tau_3 = -i \frac{k_x}{|\mathbf{k}|} \left\{ e^{\beta d_2} \left( \alpha \beta d_2 - \frac{\lambda}{(\lambda + 2\mu)} \right) - e^{\beta d_1} \left( \alpha \beta d_1 - \frac{\lambda}{(\lambda + 2\mu)} \right) \right\} F_x$$

$$-i \frac{k_y}{|\mathbf{k}|} \left\{ e^{\beta d_2} \left( \alpha \beta d_2 - \frac{\lambda}{(\lambda + 2\mu)} \right) - e^{\beta d_1} \left( \alpha \beta d_1 - \frac{\lambda}{(\lambda + 2\mu)} \right) \right\} F_y$$

$$+ \left\{ e^{\beta d_2} \left( \alpha \beta d_2 - \frac{\mu}{(\lambda + 2\mu)} - 2\alpha \right) - e^{\beta d_1} \left( \alpha \beta d_1 - \frac{\mu}{(\lambda + 2\mu)} - 2\alpha \right) \right\} F_z. \quad (\text{A7})$$

[50] 7. Construct a force couple by taking the derivative of the point source in the direction normal to the fault trace. In practice, the body forces due to the stress discontinuity across a fault plane are approximated by the derivative of a Gaussian function, effectively producing a model fault with a finite thickness (Figure A1). Curved faults are constructed with overlapping line segments having cosine tapered ends and are typically 6–10 km long.

[51] The fault trace is imbedded in a two-dimensional grid which is Fourier transformed, multiplied by the transfer functions above, equations (A5)–(A7), and inverse Fourier transformed. A constant shear modulus ( $4.12 \times 10^{10}$  Pa) and Poisson ratio (0.25) were adopted for all calculations. When the lower edge of the fault is extended to infinite depth, as in the case of the SAF system model, a Fourier cosine transform (mirrored pair) is used in the across-fault direction to maintain the far-field velocity  $\mathbf{V}$  step across the plate boundary, effectively conserving moment within the grid. Note that this requires the velocity difference (i.e., stress drop) across a system of connecting faults to have a constant value  $\mathbf{F} = \mu \mathbf{V}$ . To avoid Fourier artifacts where the fault enters the bottom of the grid and leaves the top of the grid, the fault is extended beyond the top of the model and angled to match the intersection point at the bottom (Figure A1). In addition to

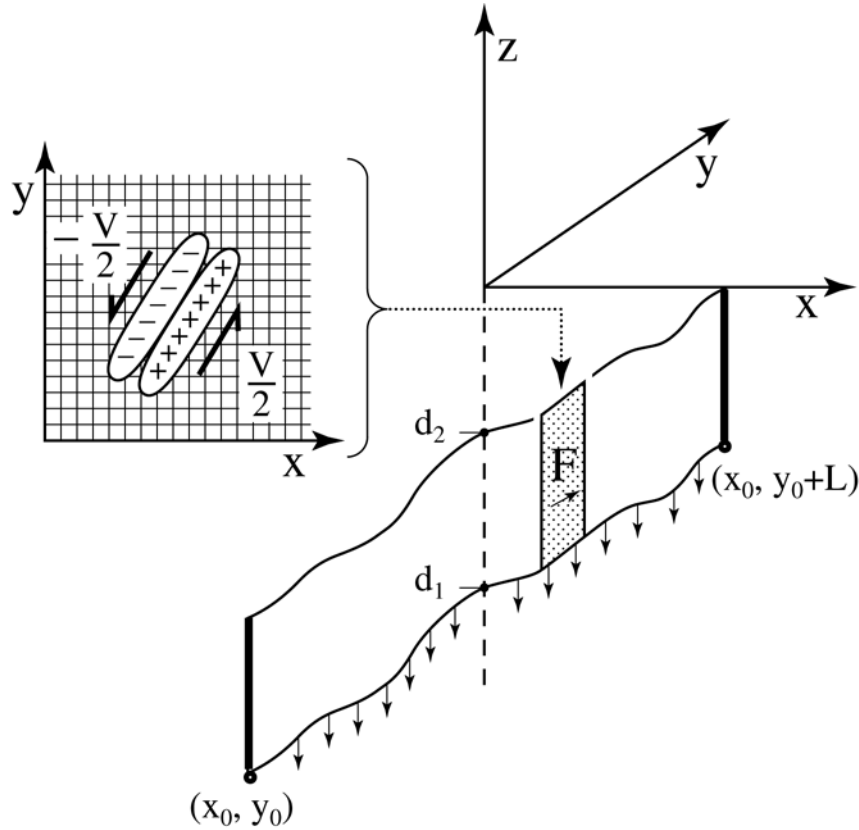


**Figure A1.** Sketch of 3-D fault model in an elastic half-space. The fault extends from a lower depth of  $d_1$  to an upper depth of  $d_2$ ; in our model,  $d_1 \rightarrow \infty$ . A displacement discontinuity across the fault is simulated using a finite width force couple,  $F$ , imbedded in the fine grid. The analytic form of the force couple is the derivative of a Gaussian function where the half width of the Gaussian is equal to the cell spacing. The solution (A4) satisfies the zero traction surface boundary condition. The  $x$  boundary condition of constant velocity difference across the plate boundary is simulated using an image fault or a cosine transform in the  $x$  direction. The  $y$  boundary condition of uniform velocity in the far-field is simulated by arranging the fault trace to be cyclic in the  $y$  dimension. That is, the slip at the end of the fault  $(x_0, y_0 + L)$  is equal to the slip at the start of the fault  $(x_0, y_0)$ .

computing the velocity field, strain and stress rates are computed from the derivatives of the model. Horizontal derivatives are computed by multiplication of  $i2\pi k$  in the Fourier transform domain and vertical derivatives are computed analytically from the transfer functions in equations (A5) and (A6).

[52] Equations (A4)–(A7) were checked using the computer algebra capabilities in Matlab and then compared to the simple arctangent function for a two-dimensional fault [Weertman, 1964]

$$V(x) = \frac{V}{\pi} \tan^{-1} \left( \frac{x}{d_2} \right).$$

Of course, in the two-dimensional case, the Boussinesq correction is not needed and equation (A5) reduces to the above arctangent formula. Figure A2 provides a numerical comparison between the above arctangent function (analytic profile) and our semianalytic Fourier solution (Fourier profile). The numerical solutions have relative errors less than 1% as long as the observation depth  $z$  is more than one grid cell size above the locking depth  $d_2$ .

[53] The numerical approach is very efficient; for example, writing and displaying of the deformation/stress grids

requires more computer time than the actual computation of the model. The horizontal complexity of the fault system has no effect on the speed of the computation. However, variations in locking depth along the fault system require computing the model for each different locking depth and summing the outputs to form the full solution. The extension to a viscoelastic half-space would not introduce a computational burden on an ordinary workstation.

## Appendix B: Locking Depth Analysis of Individual Fault Segments

[54] We estimate lower locking depth for each of the 18 fault segments of the SAF system using a least squares fit to 1099 GPS-derived horizontal velocities (Figure 2) and an assigned cumulative deep slip rate of 40 mm/yr (Table 1). In some cases, as addressed below, locking depth results proved larger than previously published studies. We attribute this behavior to both lack of geodetic data and a slight overestimate in assigned slip rate, due to the omission of external active faults within the region that tend to absorb some of the plate boundary motion. Hence a larger applied plate velocity

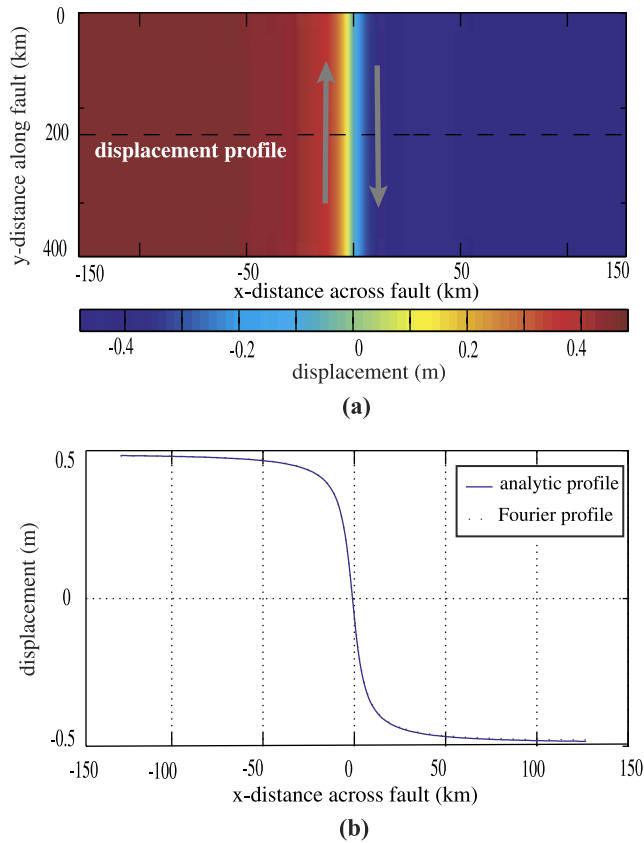


**Figure A2.** Example model output with arctangent function comparison. (a) Map view of an infinitely long fault in the  $y$  dimension imbedded in a 1-km spaced grid. We have assigned an upper locking depth of 5 km ( $d_2$ ) to the fault plane and have extended the lower depth to infinity ( $d_1$ ). (b) Comparison between the analytic solution of Weertman [1964] and a fault-perpendicular profile of our semianalytic Fourier model. The two solutions are virtually indistinguishable and have relative errors less than 1%.

is effectively compensated by deeper locking of SAF fault segments. However, applying a deep slip rate other than 40 mm/yr does not significantly improve the fit to the GPS data, and yields inconsistent long-term slip rates for individual fault segments [WGCEP, 1995, 1999]. The locking depth results of our best fitting model are summarized below.

### B1. Profile 1, Segment 1

[55] The Imperial fault, shown in Profile 1 of Figure 2b, is best modeled by a locking depth of  $5.9 \pm 1.2$  km. Published values of locking depth for the Imperial fault range from 8 to 13 km [Archuleta, 1984; Genrich and Bock, 1997; Lyons *et al.*, 2002], typically accompanying 45 mm/yr of slip with variations of surface creep. Genrich and Bock [1997] argue for a 9 km locking depth but also cite 5 km as a reasonable minimum. Seismicity locations are identified at depths of  $7.5 \text{ km} \pm 4.5 \text{ km}$  [Richards-Dinger and Shearer, 2000], lending equal validity to our more shallow locking depth estimate.

[56] The Imperial fault is known to exhibit fairly complex slip behavior with associated creep and perhaps cannot be accurately modeled as a single fault segment that is simply

locked at depth. Because we do not included the effects of shallow creep into our analysis, it is possible that our model is forced to shallower locking depths in order to satisfy data that do reflect fault creep. Conversely, the improved SCEC velocities may actually reveal the nature of a more shallowly locked fault than that of previous published models of the Imperial fault based on earlier data. It is also possible that the Imperial segment has a significant dipping component, producing an asymmetric displacement [Lyons *et al.*, 2002]. Our model neglects the case of dipping faults as we assume that all segments of the SAF system are vertical fault planes.

### B2. Profile 2, Segments 2 and 4

[57] Profile 2 compares velocities of both the Brawley segment and Borrego segment. Our inversion results in a locking depth estimate of  $6.3 \pm 1.3$  km for the Brawley region. Johnson and Hadley [1976] identified hypocentral depths of earthquake swarms in the 4–8 km range for this region, placing our solution within acceptable range. Similarly, Johnson *et al.* [1994] present a 5 km locking depth model for the Brawley region based on work by Bird and Rosenstock [1984], Weldon and Sieh [1985], Rockwell *et al.* [1990], and Sieh and Williams [1990]. Data are fairly sparse in the Borrego region, as evident in Profile 2, and do not show significant evidence for fault deformation, resulting in a locking depth of  $2.0 \pm 7.7$  km. Our model produced rather unstable results for this segment, often leaning toward 0 km locking depth. We attribute this behavior to not only lack of data, but also the fact that the fault trace of this region was estimated by connecting the lower Anza segment with the upper Imperial fault trace. In this region, many small sub-parallel branches exist [Larsen *et al.*, 1992] and we have most likely oversimplified the fault geometry. Seismicity is not particularly evident within 10 km of our estimated fault trace, and is found primarily to the southwest and constricted to the upper 10 km of the crust [Hill *et al.*, 1991]. Johnson *et al.* [1994] show seismicity clustered heavily in the upper 5 km of the crust for the southernmost portion of our modeled region. They also identify a 5 km shallow locking depth solution for this region from geodetic observations.

### B3. Profile 3, Segments 3 and 5

[58] Profile 3 displays the major region of the San Jacinto and Coachella-San Bernardino fault segments (Figure 1, segments 5 and 3, respectively). We find a locking depth of  $22.6 \pm 1.7$  km for the greater portion of the Coachella-San Bernardino segment, providing a good match to the 25 km depth chosen by Feigl *et al.* [1993]. The San Jacinto region is best modeled at  $13.1 \text{ km} \pm 2.3 \text{ km}$ , corresponding within limits of uncertainty to the 10–11 km locking depth estimated by previous models [Sanders, 1990; Savage, 1990; Li and Lim, 1988]. Seismicity is heavily confined to 10–20 km depths for the San Jacinto region [Johnson *et al.*, 1994], placing our modeled estimate of 13 km within acceptable limits. A visual inspection of Profile 3 also reveals the anomalous velocities associated with regional deformation due to the Eastern California Shear Zone (ECSZ), located east of the San Bernardino-Coachella trace. Our modeling efforts do not account for the complex deformation evident in this region [Dokka and Travis, 1990; Sauber *et al.*, 1986; Savage, 1990], nor do we include

the left-lateral Pinto Mountain Fault into our analysis, also known to contribute additional complications in this area.

#### B4. Profile 4, Segment 6

[59] Profile 4 displays our modeled Mojave segment at  $26 \pm 1.7$  km depth. Similarly, *Eberhart-Phillips et al.* [1990] propose a 25 km locking depth for this region. *Savage* [1990] argues for a 30 km locking depth estimate for this portion of the Transverse Ranges using an elastic plate model overlying a viscoelastic half-space, providing a realistic match to our simple elastic half-space model. *Thatcher* [1983] illustrated a similar comparison for this region, making the valid point that two physically different mechanisms (elastic vs. viscoelastic half-space) produce indistinguishable surface deformation. Again, we note the evident unmodeled velocities to the east of the fault trace that are related to complex deformation patterns of the ECSZ.

#### B5. Profile 5, Segment 7

[60] The Carrizo segment, located just north of the Big Bend, is shown in Profile 5, modeled at  $25.2 \pm 2.6$  km. This value agrees well with previously published models of 25 km locking depth [*Eberhart-Phillips et al.*, 1990]. We again note anomalous velocities to the east of this region, consistent with Eastern California Shear Zone deformation.

#### B6. Profile 6, Segment 8

[61] The Cholame segment, located in Profile 6, is modeled best by a locking depth of  $12.7 \pm 2.4$  km. Similarly, *Richards-Dinger and Shearer* [2000] note seismicity located down to 12.5 km for this segment. *King et al.* [1987] prefer a model with a deep slip rate of 33 mm/yr and a locking depth of 16 km for this region, but also discuss the potential for locking between 14 and 18 km for constrained deep slip of 36 mm/yr. Our estimate of  $12.7 \pm 2.4$  km places our results within reasonable agreement, although we constrain our deep slip at 40 mm/yr for this segment. Alternatively, *Li and Lim* [1988] explore shallow locking depths (4–9 km) as a plausible fit to the Cholame region.

#### B7. Profile 7, Segment 9

[62] The Parkfield segment is shown in Profile 7, modeled at  $14.5 \pm 2.9$  km locking depth. It should be noted that the Parkfield segment incorporates a transitioning region of slip from a locked fault to that of aseismic creep [*Harris and Segall*, 1987]. Because this slip transition occurs along the 25 km length of the fault segment, our model finds a minimized misfit relating to the deeper locked portion to the south. *Harris and Segall* [1987] also report a 14 km transition depth for the locked portion of the Parkfield segment. Our model estimate and uncertainty lie slightly deeper than the 8–10 km locking depth published by *King et al.* [1987] but within uncertainty limits of the locking depth estimate of *Eaton et al.* [1970] of 10–12 km from aftershocks of the 1966 earthquake that occurred along the fault. *Richards-Dinger and Shearer* [2000] provide seismicity depths ranging from  $11.4 \pm 6.7$  km.

#### B8. Profile 8, Segment 10

[63] Profile 8 shows our result for the creeping section of the SAF, just north of the Parkfield segment. Our inversion provides a locking depth of  $1.3 \pm 0.2$  km, which does

not imply continuous or quasi-continuous slip (fault creep) at the surface, as would be expected from geologic and geodetic estimates [*Savage and Burford*, 1973; *Thatcher*, 1979]. Data coverage is rather weak for this region, and it is possible that the geodetic measurements used in our analysis do not completely capture the true behavior of aseismic surface creep.

#### B9. Profile 9, Segments 11 and 13

[64] Profile 9 displays modeled segments of the San Andreas (Santa Cruz and Peninsula) fault along with the Southern and Central Calaveras fault. We find that a  $9.3 \pm 0.6$  km locking depth for the San Andreas region satisfies the data well, corresponding nicely to the 10 km estimate used by *Feigl et al.* [1993], and within acceptable limits to the estimate of 12 km by *Murray and Segall* [2001]. The Calaveras fault, located to the east of the San Andreas fault trace, exhibits regions of aseismic slip as it branches off in the northeastward direction from the creeping portion of the main San Andreas strand. This segment is known to have a high creep rate of 12–17 mm/yr [*WGCEP*, 1996; *Bakun*, 1999], matching its long-term slip rate. We find that a locking depth of 1.6 km is required to accurately model the geodetic data for this region. This estimate agrees with *Oppenheimer et al.*'s [1988] estimate of 1–2 km based on aftershock solutions of the Morgan Hill event of 1984.

#### B10. Profile 10, Segments 14 and 16

[65] Further north, the Calaveras fault branches into the Southern Hayward fault to the west and the Northern Calaveras-Concord faults to the east. Profile 10 illustrates this behavior and also captures the Santa Cruz-Peninsula segment of the San Andreas as discussed above. We find a locking depth of  $13.7 \pm 4.6$  km for the Northern Calaveras-Concord and  $15.7 \pm 3.7$  km for the Hayward region. While our model finds satisfactory locking depth estimates for this region, our results are rather unstable in that they tend to dramatically over and under estimate regions of the northern SAF system if left unbounded. The results we present here are most likely an unfortunate product of sparse data for this region, as illustrated by their associated uncertainties. Attempts to constrain either of these segments to a more shallow depth (e.g., 10.4 km [*Murray and Segall*, 2001] for Northern Calaveras-Concord or 12–14 km [*Burgmann et al.*, 2000; *Simpson et al.*, 2001] for Southern Hayward) simply result in unacceptably deep locking depth results for the remaining segments. Additions to the data set for the northern SAF system will be required in order to place better locking depth estimates for these regions.

#### B11. Profile 11, Segments 11, 17, and 14

[66] We obtain similar results for the segments incorporated into Profile 11. Again, we model the Santa Cruz-Peninsula segment and Northern Calaveras-Concord segment, now along with the Rodgers Creek segment. We again find a deeper locking depth than expected for the Rodgers Creek segment at  $18.9 \pm 6.7$  km. This fault segment is thought to be completely locked to the base of the seismogenic zone, exhibiting zero properties of shallow creep [*WGCEP*, 1999]. Microseismicity suggests that this fault segment extends to a depth of approximately 12 km [*Budding et al.*, 1991], while hypocentral depths of two

1969 events of the Rodgers Creek fault were estimated at 9.5 and 10.5 km depths [Steinbrugge *et al.*, 1970]. While our model estimate of this fault is admittedly higher than such published depths, our regions of uncertainty are also high, placing the modeled Rodgers Creek locking depth within acceptable limits. Again, additional data are necessary to make a better locking depth estimate of this segment.

### B12. Profile 12, Segments 12, 15, and 18

[67] Finally, we present our results for the northernmost region of the San Andreas system in Profile 12, modeling segments of North Coast San Andreas, Maacama, and Green Valley-Bartlett Springs faults. We find a  $19.4 \pm 2.1$  km locking depth best fits the North Coast section of the San Andreas Fault region, which agrees with Matthews and Segall [1993], who propose a 15–20 km locking depth. Furlong *et al.* [1989] provide a valid explanation for such deep locking behavior, suggesting that the northern San Andreas is connected to a deep shear zone by a subhorizontal detachment at approximately 20 km depth. We also find locking depth values of  $12.3 \pm 4.3$  km for the Maacama fault and  $9.1 \text{ km} \pm 8.4$  km for the Bartlett Springs fault. Unfortunately, seismicity depths are dispersed from 0 to 15 km [Castillo and Ellsworth, 1993] for the eastern region and do not help constrain our results. These three regions are well modeled by Freymueller *et al.* [1999] with locking depth estimates of 14.9 km (+12.5/–7.1 km), 13.4 km (+7.4/–4.8 km), and 0 km (+5 km) for the North Coast San Andreas, Maacama, and Green Valley-Bartlett Springs faults, respectively. While our estimates match those of Freymueller *et al.* [1999] within their limits of uncertainty, we again note that the data coverage for this region is particularly sparse and not extremely well posed for our locking depth inversion.

[68] **Acknowledgments.** We thank Duncan Agnew, Yehuda Bock, Jeff Freymueller, and Roland Burgman for providing the GPS velocity measurements and the guidance on how to use them. Yuri Fialko and Donna Blackman provided careful in-house reviews of draft versions of the manuscript. We thank Ross Stein, Jim Savage, and the Associate Editor, Massimo Cocco, for their help on improving the manuscript and clarifying the model. This research was supported by the NASA Solid Earth and Natural Hazards program (NAGS-9623) and the NSF Earth Science Program (EAR-0105896).

### References

- Archuleta, R. J., A faulting model for the 1979 Imperial Valley earthquake, *J. Geophys. Res.*, **89**, 4559–4585, 1984.
- Atwater, T., Plate tectonic history of southern California with emphasis on the Western Transverse Ranges and Santa Rosa Island, in *Contributions to the Geology of the Northern Channel Islands, Southern California*, edited by P. W. Weigand, pp. 1–8, Am. Assoc. of Pet. Geol., Pac. Sect., Bakersfield, Calif., 1998.
- Bakun, W., Seismic Activity of the San Francisco Bay Region, *Bull. Seismol. Soc. Am.*, **89**, 764–784, 1999.
- Bird, P., and R. W. Rosenstock, Kinematics of present crust and mantle flow in southern California, *Geo. Soc. Am. Bull.*, **95**, 946–957, 1984.
- Brown, R. D., Jr., Quaternary deformation, in *The San Andreas Fault System California*, edited by R. E. Wallace, *U.S. Geol. Surv. Prof. Pap.*, **1515**, 104–109, 1991.
- Budding, K. E., D. P. Schwartz, and D. H. Oppenheimer, Slip rate, earthquake recurrence, and seismogenic potential of the Rodgers Creek Fault Zone, northern California: Initial results, *Geophys. Res. Lett.*, **18**, 447–450, 1991.
- Burgmann, R., D. Schmidt, R. M. Nadeau, M. d'Alessio, E. Fielding, D. Manaker, T. V. McEvilly, and M. H. Murray, Earthquake potential along the northern Hayward fault, California, *Science*, **289**, 1178–1182, 2000.
- Byerlee, J. D., Friction of rock, *Pure Appl. Geophys.*, **116**, 615–626, 1978.
- Castillo, D. A., and W. L. Ellsworth, Seismotectonics of the San Andreas fault system between Point Arena and Cape Mendocino in northern California: Implications for the development and evolution of a young transform, *J. Geophys. Res.*, **98**, 6543–6560, 1993.
- Chinnery, M. A., The deformation of the ground around surface faults, *Bull. Seismol. Soc. Am.*, **51**, 355–372, 1961.
- Chinnery, M. A., The stress changes that accompany strike-slip faulting, *Bull. Seismol. Soc. Am.*, **53**, 921–932, 1963.
- Craymer, M. R., and P. Vanicek, Comment on “Saugus-Palmdale, California, field test for refraction error in historical leveling surveys” by R. S. Stein, C. T. Whalen, S. R. Holdahl, W. E. Strange, and W. Thatcher, and reply to “Comment on ‘Futher analysis of the 1981 Southern California field test for leveling refraction by M. R. Craymer and P. Vanicek’ by R. S. Stein, C. T. Whalen, S. R. Holdahl, W. E. Strange, and W. Thatcher”, *J. Geophys. Res.*, **94**, 7667–7672, 1989.
- DeMets, C., R. G. Gordon, D. F. Argus, and S. Stein, Current plate motions, *Geophys. J. Int.*, **101**, 425–478, 1990.
- DeMets, C., R. G. Gordon, D. F. Argus, and S. Stein, Effect of recent revisions to the geomagnetic reversal time scale on estimates of current plate motions, *Geophys. Res. Lett.*, **21**, 2191–2194, 1994.
- Dokka, R. K., and C. J. Travis, Role of the Eastern California Shear Zone in accommodating Pacific-North American plate motion, *Geophys. Res. Lett.*, **17**, 1323–1326, 1990.
- Eaton, J. P., M. E. O'Neill, and J. N. Murdock, Aftershocks of the 1966 Parkfield-Cholame, California earthquake: A detailed study, *Bull. Seismol. Soc. Am.*, **60**, 1151–1197, 1970.
- Eberhart-Phillips, D., M. Lisowski, and M. D. Zoback, Crustal strain near the Big Bend of the San Andreas fault: Analysis of the Los Padres-Tehachapi trilateration networks, California, *J. Geophys. Res.*, **95**, 1139–1153, 1990.
- Elders, W. A., R. W. Rex, T. Meidav, P. T. Robinson, and S. Biehler, Crustal spreading in Southern California, *Science*, **178**, 15–24, 1972.
- Ellsworth, W. L., Earthquake history, 1769–1989, in *The San Andreas Fault System, California*, edited by R. E. Wallace, *U.S. Geol. Surv. Prof. Pap.*, **1515**, 152–187, 1990.
- Feigl, K. L., et al., Space geodetic measurements of crustal deformation in central and southern California, 1984–1992, *J. Geophys. Res.*, **98**, 21,677–21,712, 1993.
- Fialko, Y., and M. Simons, Deformation and seismicity in the Coso geothermal area, Inyo County, California: Observations and modeling using satellite radar interferometry, *J. Geophys. Res.*, **105**, 21,781–21,794, 2000.
- Freymueller, J. T., M. H. Murray, P. Segall, and D. Castillo, Kinematics of the Pacific-North America plate boundary zone, northern California, *J. Geophys. Res.*, **104**, 7419–7441, 1999.
- Furlong, K. P., W. D. Hugo, and G. Zandt, Geometry and evolution of the San Andreas Fault Zone in northern California, *J. Geophys. Res.*, **94**, 3100–3110, 1989.
- Genrich, J. F., and Y. Bock, Crustal deformation across the Imperial Fault: Results from kinematic GPS surveys and trilateration of a densely spaced, small-aperture network, *J. Geophys. Res.*, **102**, 4985–5004, 1997.
- Harris, R. A., and P. Segall, Detection of a locked zone at depth on the Parkfield, California, segment on the San Andreas Fault, *J. Geophys. Res.*, **92**, 7945–7962, 1987.
- Harris, R., and R. Simpson, Changes in static stress on southern California faults after the 1992 Landers earthquake, *Nature*, **360**, 251–254, 1992.
- Hill, D. P., P. Mowinckel, and L. G. Peake, Earthquakes, active faults, and geothermal areas in the Imperial Valley, California, *Science*, **188**, 1306–1308, 1975.
- Hill, D. P., J. P. Eaton, and L. M. Jones, Seismicity, 1980–1986, in *The San Andreas Fault System, California*, edited by R. E. Wallace, *U.S. Geol. Surv. Prof. Pap.*, **1515**, 133–136, 1991.
- Hudnut, K. W., L. Seeber, and J. Pacheco, Cross-fault triggering in the November 1987 Superstition Hills earthquake sequence, southern California, *Geophys. Res. Lett.*, **16**, 199–202, 1989.
- Jennings, C. W., Fault activity map of California and adjacent areas with locations and ages of recent volcanic eruptions, *Data Map Ser. 6*, 92 pp., 2 plates, map scale 1:750,000, Calif. Div. of Mines and Geol., Sacramento, 1994.
- Johnson, C. E., and D. M. Hadley, Tectonic implications of the Brawley earthquake swarm, Imperial Valley, California, January 1975, *Bull. Seismol. Soc. Am.*, **66**, 1133–1144, 1976.
- Johnson, H. O., D. C. Agnew, and F. K. Wyatt, Present-day crustal deformation in southern California, *J. Geophys. Res.*, **99**, 23,951–23,974, 1994.
- Jones, L. M., Focal mechanisms and the state of stress on the San Andreas Fault in southern California, *J. Geophys. Res.*, **93**, 8869–8891, 1988.
- King, G. C. P., and M. Cocco, Fault interaction by elastic stress changes: New clues from earthquake sequences, *Adv. Geophys.*, **44**, 1–38, 2001.

- King, G. C. P., R. S. Stein, and J. Lin, Static stress changes and the triggering of earthquakes, *Bull. Seismol. Soc. Am.*, *84*, 935–953, 1994.
- King, N. E., P. Segall, and W. Prescott, Geodetic measurements near Parkfield, California, 1959–1984, *J. Geophys. Res.*, *92*, 2747–2766, 1987.
- Lachenbruch, A. H., and J. H. Sass, The stress heat-flow paradox and thermal results from Cajon Pass, *Geophys. Res. Lett.*, *15*, 981–984, 1988.
- Larsen, S. C., and R. S. Reilinger, Age constraints for the present fault configuration in the Imperial Valley, California: Evidence for northward propagation of the Gulf of California rift system, *J. Geophys. Res.*, *96*, 10,339–10,346, 1991.
- Larsen, S., R. Reilinger, H. Neubegauer, and W. Strange, Global positioning system measurements of deformations associated with the 1987 Superstition Hills earthquake: Evidence of conjugate faulting, *J. Geophys. Res.*, *97*, 4885–4902, 1992.
- Li, V. C., and H. S. Lim, Modeling surface deformations at complex strike-slip plate boundaries, *J. Geophys. Res.*, *93*, 7943–7954, 1988.
- Lisowski, M., J. C. Savage, and W. H. Prescott, The Velocity field along the San Andreas Fault in central and southern California, *J. Geophys. Res.*, *96*, 8369–8389, 1991.
- Lomnitz, C., F. Mooser, C. R. Allen, J. N. Brune, and W. Thatcher, Seismicity and tectonics of the northern gulf of California region, Mexico—Preliminary results, *Geophys. Int.*, *10*, 37–48, 1970.
- Lyons, S. N., Y. Bock, and D. T. Sandwell, Creep along the Imperial Fault, southern California, from GPS measurements, *J. Geophys. Res.*, *107*(B10), 2249, doi:10.1029/2001JB000763, 2002.
- Matthews, M. V., and P. Segall, Estimation of depth-dependent fault slip from measured surface deformation with application to the 1906 earthquake, *J. Geophys. Res.*, *98*, 12,153–12,163, 1993.
- Minster, J. B., and T. H. Jordan, Vector constraints on western U.S. deformations from space geodesy neotectonics and plate motions, *J. Geophys. Res.*, *92*, 4798–4804, 1987.
- Murray, M. H., and P. Segall, Modeling broadscale deformation in northern California and Nevada from plate motions and elastic strain accumulation, *Geophys. Res. Lett.*, *28*, 3215–3218, 2001.
- Okada, Y., Surface deformation due to shear and tensile faults in a half-space, *Bull. Seismol. Soc. Am.*, *75*, 1135–1154, 1985.
- Okada, Y., Internal deformation due to shear and tensile faults in a half-space, *Bull. Seismol. Soc. Am.*, *82*, 1018–1040, 1992.
- Oppenheimer, D. H., P. A. Reasenberg, and R. W. Simpson, Fault plane solutions of the 1984 Morgan Hill, California, earthquake sequence: Evidence for the state of stress on the Calaveras Fault, *J. Geophys. Res.*, *93*, 9007–9026, 1988.
- Parker, R. L., Nonlinear problems, in *Geophysical Inverse Theory*, pp. 293–368, Princeton Univ. Press, Princeton, N. J., 1994.
- Peterson, M., W. Bryant, C. Cramer, T. Cao, M. Reichle, A. Frankel, J. Lienkaemper, P. McCrory, and D. Schwartz, Probabilistic seismic hazard assessment for the state of California, *U.S. Geol. Surv. Open File Rep.*, *96-706*, 1–64, 1996.
- Pollitz, F. F., C. Wicks, and W. Thatcher, Mantle flow beneath a continental strike-slip fault: Postseismic deformation after the 1999 Hector Mine earthquake, *Science*, *293*, 1814–1818, 2001.
- Richards-Dinger, K. B., and P. M. Shearer, Earthquake locations in southern California obtained using source-specific station terms, *J. Geophys. Res.*, *105*, 10,939–10,960, 2000.
- Rockwell, T., C. Loughman, and P. Merifield, Late Quaternary rate of slip along the San Jacinto fault zone near Anza, southern California, *J. Geophys. Res.*, *95*, 8593–8605, 1990.
- Rybicki, K., Analysis of aftershocks on the basis of dislocation theory, *Phys. Earth Planet Inter.*, *7*, 409–422, 1973.
- Sanders, C. O., Earthquake depths and the relation to strain accumulation and stress near strike-slip faults in southern California, *J. Geophys. Res.*, *95*, 4751–4762, 1990.
- Sauber, J., W. Thatcher, and S. C. Solomon, Geodetic measurements of deformation in the central Mojave Desert, California, *J. Geophys. Res.*, *91*, 12,683–12,693, 1986.
- Savage, J. C., Equivalent strike-slip earthquake cycles in half-space and lithosphere-asthenosphere earth models, *J. Geophys. Res.*, *95*, 4873–4879, 1990.
- Savage, J. C., and R. O. Burford, Geodetic determination of relative plate motion in central California, *J. Geophys. Res.*, *78*, 832–845, 1973.
- Savage, J. C., and M. Lisowski, Inferred depth of creep on the Hayward fault, central California, *J. Geophys. Res.*, *98*, 787–793, 1993.
- Savage, J. C., and R. W. Simpson, Surface strain accumulation and the seismic moment tensor, *Bull. Seismol. Soc. Am.*, *87*, 1345–1353, 1997.
- Savage, J. C., W. H. Prescott, M. Lisowski, and N. King, Deformation across the Salton Trough, California, 1973–1977, *J. Geophys. Res.*, *84*, 3069–3079, 1979.
- Sieh, K. E., and P. L. Williams, Behavior of the southernmost San Andreas Fault during the past 300 years, *J. Geophys. Res.*, *95*, 6629–6645, 1990.
- Simpson, R. W., and P. A. Reasenberg, Earthquake-induced static stress changes on central California faults, *U.S. Geol. Surv. Prof. Pap., Rep. P 1550-F*, F55–F89, 1994.
- Simpson, R. W., J. J. Lienkaemper, and J. S. Galehouse, Variations in creep rate along the Hayward Fault, California, interpreted as changes in depth of creep, *Geophys. Res. Lett.*, *28*, 2269–2271, 2001.
- Stein, R. S., Contemporary plate motion and crustal deformation, *Rev. Geophys.*, *25*, 855–863, 1987.
- Stein, R. S., and M. Lisowski, The 1979 Homestead Valley earthquake sequence, California: Control of aftershocks and postseismic deformation, *J. Geophys. Res.*, *88*, 6477–6490, 1983.
- Stein, R. S., G. C. P. King, and J. Lin, Stress triggering of the 1994  $M = 6.7$  Northridge, California, earthquake by its predecessors, *Science*, *265*, 1432–1435, 1994.
- Steinbrugge, K. V., W. K. Cloud, and N. H. Scott, The Santa Rosa, California, earthquakes on October 1, 1969, vol. 1970, pp. 1–63, U.S. Environ. Sci. Serv. Admin., Silver Spring, Md., 1970.
- Steketee, J. A., On Volterra's dislocations in a semi-infinite elastic medium, *Can. J. Phys.*, *36*, 192–205, 1958.
- Thatcher, W., Systematic inversion of geodetic data in central California, *J. Geophys. Res.*, *84*, 2283–2295, 1979.
- Thatcher, W., Nonlinear strain buildup and the earthquake cycle on the San Andreas Fault, *J. Geophys. Res.*, *88*, 5893–5902, 1983.
- Ward, S. N., Pacific-North America plate motions: New results from very long baseline interferometry, *J. Geophys. Res.*, *95*, 21,965–21,981, 1990.
- Ward, S. N., A multidisciplinary approach to seismic hazard in southern California, *Bull. Seismol. Soc. Am.*, *84*, 1293–1309, 1994.
- Wdowinski, S., Y. Sudman, and Y. Bock, Geodetic detection of active faults in S. California, *Geophys. Res. Lett.*, *28*, 2321–2324, 2001.
- Weldon, R. J., II, and K. E. Sieh, Holocene rate of slip and tentative recurrence interval for large earthquakes on the San Andreas Fault, Cajon Pass, southern California, *Bull. Seismol. Soc. Am.*, *96*, 793–812, 1985.
- Weertman, J., Continuum distribution of dislocations on faults with finite friction, *Bull. Seismol. Soc. Am.*, *54*, 1035–1058, 1964.
- Williams, C. A., and R. M. Richardson, A rheologically layered three-dimensional model of the San Andreas Fault in central and southern California, *J. Geophys. Res.*, *96*, 16,597–16,623, 1991.
- Working Group on California Earthquake Probabilities (WGCEP), Seismic hazards in southern California: Probable earthquakes, 1994 to 2024, *Bull. Seismol. Soc. Am.*, *85*, 379–439, 1995.
- Working Group on California Earthquake Probabilities (WGCEP), Earthquake probabilities in the San Francisco Bay Region: 2000 to 2030—A summary of Findings, *U.S. Geol. Surv. Open File Rep.* [Online], 99-517, version 1.0, 1999.
- Working Group on Northern California Earthquake Potential (WGNCEP), Database of potential sources for earthquakes larger than magnitude 6 in northern California, *U.S. Geol. Surv. Open File Rep.*, *96-705*, 1996.
- Yule, D., and K. Sieh, Neotectonic and paleoseismic investigation of the San Andreas fault system, San Geronio Pass, *1996 SCEC Annu. Rep. 14-08-001-A0899 C*, pp. 70–74, South. Calif. Earthquake Cent., Los Angeles, Calif., 1997.
- Zeng, Y., Viscoelastic stress-triggering of the 1999 Hector Mine earthquake by the 1992 Landers earthquake, *Geophys. Res. Lett.*, *28*, 3007–3010, 2001.

D. Sandwell and B. Smith, Institute for Geophysics and Planetary Physics, Scripps Institution of Oceanography, 9500 Gilman Drive, Mail Code 0255, La Jolla, CA 92093-0255, USA. (dsandwell@ucsd.edu; bsmith@igpp.ucsd.edu)